THE JOURNAL OF BIOLOGICAL CHEMISTRY VOL. 289, NO. 46, pp. 32214–32229, November 14, 2014

Structural and Biochemical Characterization of *Chlamydia trachomatis* Hypothetical Protein CT263 Supports That Menaquinone Synthesis Occurs through the Futalosine Pathway*

Received for publication, July 8, 2014, and in revised form, September 22, 2014 Published, JBC Papers in Press, September 24, 2014, DOI 10.1074/jbc.M114.594325

Michael L. Barta[‡], Keisha Thomas[§], Hongling Yuan[§], Scott Lovell[¶], Kevin P. Battaile[‖], Vern L. Schramm[§], and P. Scott Hefty[‡1]

From the [‡]Department of Molecular Biosciences, University of Kansas, Lawrence, Kansas 66045, the [§]Department of Biochemistry, Albert Einstein College of Medicine of Yeshiva University, Bronx, New York 10461, the [¶]Protein Structure Laboratory, Del Shankel Structural Biology Center, University of Kansas, Lawrence, Kansas 66047, and the [‖]Industrial Macromolecular Crystallography Association-Collaborative Access Team, Hauptman-Woodward Medical Research Institute, Argonne, Illinois 60439

Background: Specific pathways and components for respiration in *Chlamydia* are poorly understood.
Results: The *C. trachomatis* hypothetical protein CT263 crystal structure displays strong structural similarity with 5′-methylthioadenosine nucleosidase enzymes.
Conclusion: Bioinformatic analyses and enzymatic characterization of CT263 suggest menaquinone biosynthesis proceeds through the futalosine pathway in Chlamydiaceae.
Significance: Unique structural aspects of the CT263 active site can be leveraged to modify existing transition state inhibitors.

The obligate intracellular human pathogen *Chlamydia trachomatis* is the etiological agent of blinding trachoma and sexually transmitted disease. Genomic sequencing of *Chlamydia* indicated this medically important bacterium was not exclusively dependent on the host cell for energy. In order for the electron transport chain to function, electron shuttling between membrane-embedded complexes requires lipid-soluble quinones (*e.g.* menaquionone or ubiquinone). The sources or biosynthetic pathways required to obtain these electron carriers within *C. trachomatis* are poorly understood. The 1.58Å crystal structure of *C. trachomatis* hypothetical protein CT263 presented here supports a role in quinone biosynthesis. Although CT263 lacks sequence-based functional annotation, the crystal structure of CT263 displays striking structural similarity to 5′-methylthioadenosine nucleosidase (MTAN) enzymes. Although CT263 lacks the active site-associated dimer interface found in prototypical MTANs, co-crystal structures with product (adenine) or substrate (5′-methylthioadenosine) indicate that the canonical active site residues are conserved. Enzymatic characterization of CT263 indicates that the futalosine pathway intermediate 6-amino-6-deoxyfutalosine ($k_{cat}/K_m = 1.8 \times 10^3$ M^{-1} s^{-1}), but not the prototypical MTAN substrates (*e.g. S*-adenosylhomocysteine and 5′-methylthioadenosine), is hydrolyzed. Bioinformatic analyses of the chlamydial proteome also support the futalosine pathway toward the synthesis of menaquinone in Chlamydiaceae. This report provides the first experimental support for quinone synthesis in *Chlamydia*. Menaquinone synthesis provides another target for agents to combat *C. trachomatis* infection.

Quinones are lipid-soluble electron carriers essential to cellular respiration in bacteria (1). Although certain bacteria (*e.g. Escherichia coli*) utilize different quinones depending on oxygen availability, many Gram-negative and most Gram-positive bacteria rely on menaquionone (MK)[2] as the sole electron carrier (2). In higher order eukaryota, MK (also known as vitamin K_2) is a cofactor required for post-translational glutamate modification essential to a variety of regulatory pathways, including blood coagulation and bone metabolism (3). As humans are incapable of synthesizing MK, bacterial enzymes involved in this pathway are potential targets for the development of novel antimicrobial therapeutics.

Two distinct biosynthetic routes of MK have been described in bacteria (Fig. 1), the well studied traditional route (4, 5) and the recently discovered futalosine route (6). Both routes begin with chorismate and involve common enzymes at several of the later steps. Importantly, no organism has been found to possess a complete set of enzymes required for both the traditional and futalosine MK biosynthetic routes (6). Thus, the presence of genes unique to either pathway indicates that complete routes are encoded. Human commensal bacteria, primarily facultative anaerobes (*e.g. Lactobacillus*), typically do not synthesize MK

* This work was supported, in whole or in part, by National Institutes of Health Grants AI079083 and GM041916.
The atomic coordinates and structure factors (codes 4QAQ, 4QFB, 4QAR, 4QAS, and 4QAT) have been deposited in the Protein Data Bank (http://wwpdb.org/).
[1] To whom correspondence should be addressed: 1200 Sunnyside Ave., University of Kansas, Lawrence, KS 66045. Tel.: 785-864-5392; Fax: 785-864-5294; Email: pshefty@ku.edu.

[2] The abbreviations used are: MK, menaquionone; MTAN, 5′-methylthioadenosine nucleosidase; MTA, 5′-methylthioadenosine; r.m.s.d., root mean square deviation; SeMet, selenomethionine; AdoHcy, *S*-adenosylhomocysteine; AFL, 6-amino-6-deoxyfutalosine; BisTris, 2-[bis(2-hydroxyethyl)-amino]-2-(hydroxymethyl)propane-1,3-diol; PDB, Protein Data Bank; ADE, adenine; UQ, ubiquinone; AdoMet, *S*-adenosylmethionine; DHFL, dehypoxanthinyl futalosine; LCCA, last common chlamydial ancestor; BS^3, bis(sulfosuccinimidyl)suberate.

(7), and those that do (*e.g. E. coli*) utilize the traditional route. The absence of futalosine genes in these organisms strengthens the development of antimicrobial compounds targeting pathogenic bacteria that synthesize MK (8).

Chlamydia are obligate intracellular bacteria and include pathogenic species for which the requisite electron transport quinone is undetermined. The metabolically active form of *Chlamydia* replicates within a microaerophilic environment inside a modified intracellular vacuole (9). Early speculation suggested that *Chlamydia* acquire ubiquinone (UQ) from the host (10). However, genome sequencing indicated otherwise, revealing the presence of four UQ biosynthesis homologs that could play a role in quinone synthesis. As these predicted enzymes could potentially catalyze reactions found in both UQ and MK biosynthetic pathways, the predicted quinone biosynthetic pathway of *Chlamydia* has remained undefined. Previous reports suggested that *Chlamydia* possess futalosine enzyme homologs (8, 11), but these genes were not specifically described. Here, we present structural, enzymatic, and bioinformatic evidence in support of Chlamydiaceae utilizing the futalosine route toward the synthesis of MK.

EXPERIMENTAL PROCEDURES

Cloning, Overexpression, and Purification of Recombinant CT263 from Chlamydia trachomatis—A gene fragment encoding the entire open reading frame (residues 1–196) of *ctl0515* was amplified from *C. trachomatis* (serovar L2 434/Bu) genomic DNA via PCR and subcloned into BamHI/NotI-digested pT7HmT (12). In keeping with consistent chlamydial nomenclature, all references to this gene product will utilize the *C. trachomatis* D/UW-3 homolog CT263. CTL0515 and CT263 are 99% identical, with a single substitution (A76G) at the amino acid level. Upon DNA sequence confirmation, the vector was transformed into BL21(DE3) *E. coli* competent cells. This strain was grown to an A_{600} of 0.8 at 37 °C within Terrific Broth supplemented with kanamycin (50 μg/ml), and protein expression was induced overnight at 16 °C by the addition of isopropyl 1-thio-β-D-galactopyranoside to a 1 mM final concentration. Bacterial cells were harvested by centrifugation, resuspended in lysis buffer (20 mM Tris-HCl (pH 8.0), 500 mM NaCl, and 10 mM imidazole), and then lysed by sonication. The soluble His_6-labeled protein was collected in the supernatant following centrifugation of the cell homogenate and purified on a Ni^{2+}-nitrilotriacetic acid-Sepharose column according to published protocols (12). Recombinant tobacco etch virus protease was used to digest the fusion affinity tag from the target protein. Both the affinity tag and tobacco etch virus protease were removed by reverse Ni^{2+}-nitrilotriacetic acid-Sepharose chromatography. After desalting into 20 mM Tris-HCl (pH 8.0), final purification was achieved by ResourceQ anion-exchange chromatography followed by size exclusion chromatography (GE Healthcare). The purified protein was concentrated to 10 mg/ml in 20 mM Tris-HCl (pH 8.0), 200 mM NaCl buffer by ultrafiltration and stored at 4 °C for further use.

Selenomethionine (SeMet)-substituted CT263 was grown according to standard protocols (13), purified as described above (all buffers contained 5 mM β-mercaptoethanol), and concentrated to 10 mg/ml in 20 mM Tris-HCl (pH 8.0), 200 mM NaCl buffer for crystallization.

Crystallization—Recombinant *C. trachomatis* CT263 was crystallized by vapor diffusion in Compact Jr. (Emerald Biosystems) sitting drop plates at 20 °C. Specifically, 0.5 μl of protein solution (10 mg/ml in 20 mM Tris-HCl (pH 8.0), 200 mM NaCl) was mixed with 0.5 μl of reservoir solution containing 200 mM ammonium sulfate, 100 mM sodium acetate trihydrate (pH 4.6), and 30% (w/v) PEG 2K MME from the Crystal HT screen condition F1 (Hampton) and equilibrated against 75 μl of the latter. Single rectangular prism-shaped crystals appeared after 1 day and continued to grow for ~4 days. Crystals were flash-cooled in a cryoprotectant solution consisting of mother liquor with 20% (v/v) glycerol. Gold-derivatized CT263 crystals were generated by incubating native crystals for 24–48 h in mother liquor supplemented with 10 mM K_2AuCl_4. Crystals that had changed to a yellow color (indicating the likely presence of ordered gold atoms) were harvested as described above.

SeMet-CT263 crystals were obtained in essentially the same manner as wild type; however, small block-shaped crystals required reduced ammonium sulfate concentrations as well as increased pH and PEG 2K MME. Briefly, protein solution (0.5 μl) was mixed with 0.5 μl of reservoir solution (50 mM ammonium sulfate, 100 mM BisTris (pH 6.4), and 32% (w/v) PEG 2K MME) and equilibrated against 100 μl of the latter. Small block-shaped crystals were harvested as described above.

Ligand-bound CT263 crystals were obtained in a similar manner as wild type. Briefly, CT263 (wild-type or D161N, 10 mg/ml) was incubated with 10 mM MTA on ice for 30 min prior to crystallization. The ligand/protein solution (0.5 μl) was then mixed with 0.5 μl of reservoir solution (200 mM ammonium sulfate, 100 mM sodium acetate trihydrate (pH 4.6) and 30% (w/v) PEG 2K MME) and equilibrated against 100 μl of the latter. Large block-shaped crystals were harvested in a similar manner as described above.

Diffraction Data Collection, Structure Determination, Refinement, and Analysis—X-ray diffraction data were collected on all CT263 crystals at 1.000 Å at 100 K with the exception of CT263-Au and SeMet-CT263 crystals, which were collected at 1.03969 Å and 0.97911 Å, respectively, using a Dectris Pilatus 6 M pixel array detector at IMCA-CAT beamline 17ID at the APS (Table 2). Following data collection, individual reflections from each dataset were integrated with XDS (14). Laue class analysis and data scaling were performed with Aimless (15), which suggested the Laue class was *mmm*. Systematic absences were analyzed and suggested that the likely space group was $P22_12_1$ for all datasets with the exception of SeMet-CT263 ($P2_122_1$). The axes were permuted to $P2_12_12$ using Reindex Reflections in CCP4 (16) for all datasets, except SeMet-CT263, to adopt standard space group nomenclature.

Experimental phase information was obtained for the CT263 structure by Au-SAD using AutoSol within the Phenix suite (17, 18), which identified two unique gold atoms in the asymmetric unit. Phenix.Autobuild correctly traced 269/392 Cα atoms (Map-model CC = 0.70, R_{work}/R_{free} = 38.57/43.00) within two CT263 polypeptides. Anomalous phases were combined with the complete 1.58 Å diffraction dataset using CAD (16). Subsequently, Phenix.Autobuild (17, 18) was then used to

trace 309/392 of the expected amino acids from the combined experimental maps with R_{work}/R_{free} = 26.74/29.77.

The structure of SeMet-CT263 was independently determined by Se-SAD using AutoSol within the Phenix suite (17, 18), which identified eight unique selenium atoms in the asymmetric unit. Phenix.Autobuild correctly traced 353/392 Cα atoms (Map-model CC = 0.85, R_{work}/R_{free} = 21.00/24.98) within two CT263 polypeptides. Chains A and B of Protein Data Bank (PDB) entry 4QAQ (wild-type *C. trachomatis* CT263) were used as a search model for WT/ADE, apo-CT263^{D161N}, and CT263^{D161N}-MTA structures.

Structural refinement was carried out using Phenix (17, 18) for all structures. One round of individual coordinates and isotropic atomic displacement factor refinement was conducted, and the refined model was used to calculate both $2F_o - F_c$ and $F_o - F_c$ difference maps. These maps were used to iteratively improve the model by manual building with Coot (19, 20) followed by subsequent refinement cycles. TLS refinement (21) was incorporated in the final stages to model anisotropic atomic displacement parameters. Ordered solvent molecules were added according to the default criteria of Phenix and inspected manually using Coot prior to model completion. Interpretable electron density was absent for the following residues in each structure: apo-WT, chain A, 196 and chain B, 96–101 and 195–196; apo-D161N, chain B, 97–101, 129–130, and 195–196; SeMet-CT263, chain A, 195–196 and chain B, 97–101, 124–126 and 195–196; WT/ADE, chain A, 196, chain B, 96–102 and 195–196; D161N/MTA, chain A, 196 and chain B, 97–100 and 195–196. Disordered side chains were truncated to the point where electron density could be observed. Additional information and refinement statistics are presented in Table 2.

Enzymatic Assay of CT263—Enzymatic assays were performed in 50 mM HEPES (pH 7.4), 200 mM KCl, 5% (v/v) glycerol and initiated by the addition of recombinant CT263. CT263 was added to a 200-μl reaction volume at a final concentration of 250 nM. Enzymatic activity was tested against 50 μM of the following substrates: 6-amino-6-deoxyfutalosine (AFL), *S*-adenosylhomocysteine (AdoHcy), 5′-methylthioadenosine (MTA), and adenosine triphosphate (ATP). Samples were incubated overnight at room temperature and assayed via HPLC. Product peaks were collected, dried on a speed vacuum, and analyzed by mass spectroscopy.

Characterization of Steady-state Kinetic Parameters—Activity with AFL was continuously monitored by UV-visible spectrophotometry at 263 nm. Reactions were performed in 1-ml volumes under similar reaction conditions as above with varying concentrations of AFL. Reactions were initiated by the addition of CT263 to final concentrations of 100–200 nM. A luciferase-coupled assay converted product adenine to ATP in 100 mM Tris-HCl (pH 7.7) (22). Briefly, luminescence was converted to picomoles of adenine (correcting for background and fitted to a standard curve). Initial rate kinetics (substrate k_{cat} and K_m) were calculated by fitting to the Michaelis-Menten equation.

Multiple Sequence Alignments and Figure Modeling—Multiple sequence alignments were carried out using ClustalW (23) and aligned with secondary structural elements using ESPRIPT (24). Sequences identified by DALI analysis of the CT263 crystal structure and used in alignments, along with their respective GenBank™ accession numbers, were as follows: *C. trachomatis* serovar L2 434/Bu (166154474); *Chlamydia muridarum* Nigg (15835152); *Chlamydia felis* Fe-C/56 (89898433); *Chlamydia caviae* GPIC (29840145); *Chlamydia pneumoniae* CWL029 (4376692); *Chlamydia psittaci* 6BC (332287326); *Chlamydia pecorum* (566141550); *Helicobacter pylori* (15644719); *Arabidopsis thaliana* (332661576); *Francisella philomiragia* (167626574); *Sulfurimonas denitrificans* (78777589); *Staphylococcus aureus* (15924589); *Streptococcus pneumoniae* (15900866); *Vibrio cholerae* (9656950); *Neisseria meningitidis* (15676665); *Salmonella enterica* (322713231) and *Escherichia coli* (1786354). Three-dimensional structures were superimposed using the Local-Global Alignment method (25). The following MTAN structures were obtained from the PDB (26): *E. coli* (1Z5P), *V. cholerae* (3DP9), *N. meningitidis* (3EEI), *S. pneumoniae* (3MMS), *H. pylori* (4BMZ), *S. enterica* (4F1W), *S. aureus* (4GMH), *F. philomiragia* (4JOS), and *S. denitrificans* (4JWT). Representations of all structures were generated using PyMOL (27). Calculations of electrostatic potentials at the molecular surface were carried out using DELPHI (28). The program CONSURF was used to plot levels of amino acid sequence conservation on the molecular surface (29).

RESULTS

Bioinformatic Support of Futalosine Pathway in Chlamydiaceae—The medically important human pathogen *C. trachomatis* is capable of oxidative level phosphorylation, generating ATP through the electron transport chain (30). However, the source of electron shuttling quinones has been unclear and is further compounded by the presence of four genes with homology to enzymes common to both the UQ and MK biosynthetic pathways (10). Recently, an alternative pathway toward the synthesis of MK (Fig. 1), named the futalosine pathway after the first metabolic intermediate, was described (6). This pathway was found in bacteria, including *Streptomyces*, *Helicobacter,* and *Campylobacter* among others, that had previously incomplete UQ or MK biosynthetic routes.

Iterative BLAST searches of *Streptomyces* genes involved in the futalosine pathway against available *Chlamydia* genome sequences yielded statistically significant hits for 7 of the 8 enzymes (Table 1), with only the nucleosidase step (fulfilled by MqnB or MTAN) lacking an identified homolog. As reported previously (31), despite utilizing *S*-adenosylmethionine (AdoMet) in a multitude of pathways, *Chlamydia* paradoxically appear to lack the MTAN enzyme needed to salvage products of AdoMet-utilizing reactions.

Analysis of the *C. trachomatis* transcriptome indicates that several of the BLAST-identified futalosine genes are co-transcribed (32). CT263, a protein of unknown function, is co-transcribed along with the predicted MqnD homolog (CT262). However, BLAST analysis of CT263 fails to identify a single protein of significant similarity outside of *Chlamydia*. As *Chlamydia* are phylogenetically distinct bacteria, we hypothesized that despite an absence of sequence similarity, CT263 could fulfill the nucleosidase enzymatic role (*e.g. step 2* in Fig. 1) and complete the futalosine pathway.

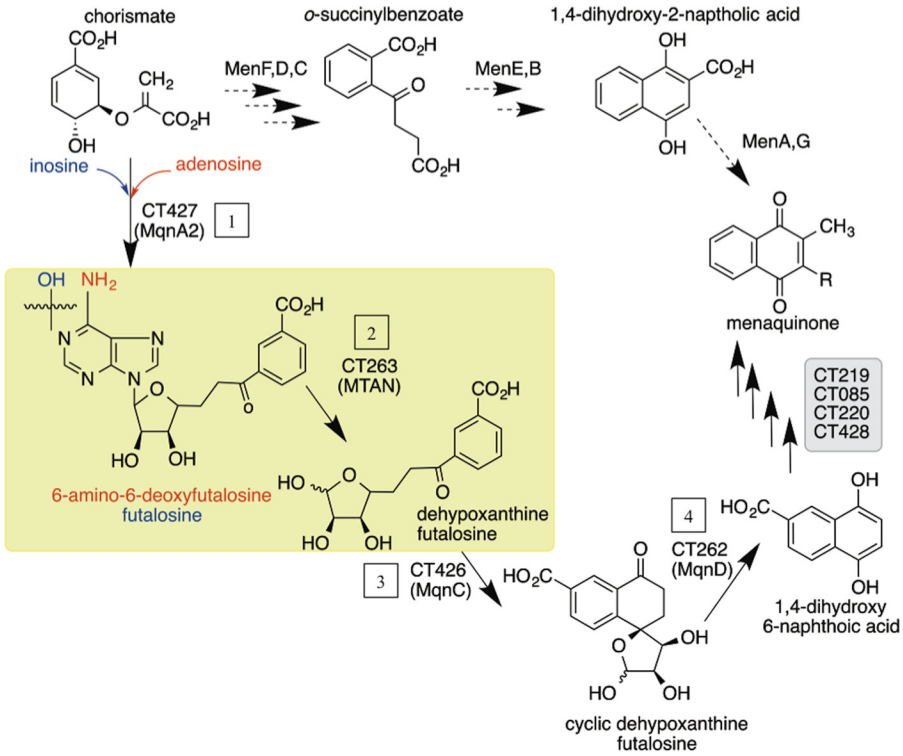

FIGURE 1. **Multiple routes toward synthesis of menaquinone in bacteria.** The traditional route of menaquinone biosynthesis has been extensively characterized in *E. coli* and involves seven Men family enzymes (*upper*). The futalosine route diverges in the first two steps as indicated by *blue* and *red* coloring for routes described in *Streptomyces coelicolor*/*Thermus thermophilus* and *C. jejuni*/*H. pylori*, respectively. Menaquinone biosynthesis in *C. trachomatis* (*CT*) is predicted to function with the genes for each step indicated (*lower*; *numbered boxes*). The *yellow-boxed* reaction represents the reaction catalyzed by CT263 studied herein. The *gray-boxed genes* represent *ubi*/*men* homologs with predicted prenylation (CT219), methylation (CT428), and decarboxylation activity (CT085 and CT220) that could function in the final steps of menaquinone synthesis.

TABLE 1

Bioinformatic analysis of futalosine biosynthesis genes in Chlamydia

Futalosine gene	Function	*Chlamydia* genes		BLAST E-value	Sequence identity	Query cover
					%	%
SCO4506[a]	MqnA	CT427[b]	CTL0686[c]	7.00E-12	21	95
SCO4327	MqnB	NA[d]	NA			
SCO4550	MqnC	CT767	CTL0136	1.00E-84	40	85
		CT426	CTL0685	2.00E-55	33	87
SCO4326	MqnD	CT262	CTL0514	4.00E-43	33	91
SCO4556	???[e]	CT428	CTL0687	4.00E-36	36	92
SCO4491	???	CT219	CTL0471	2.00E-36	36	78
SCO4490	???	CT085	CTL0340	2.00E-72	35	90
SCO4492	???	CT220	CTL0472	3.00E-23	28	94
Cj1285c[f]	MqnA2	CT427	CTL0686	1.00E-06	25	64
Cj0117	MTAN	NA	NA			

[a] SCO means *S. coelicolor* A3 (2).
[b] CT means *C. trachomatis* D/UW-3.
[c] CTL means *C. trachomatis* L2 434/Bu.
[d] NA means not applicable.
[e] ??? means genes predicted to be involved in Futalosine pathway by sequence homology (6).
[f] Cj means *C. jejuni.*

Despite annotation as a protein of unknown function, the NCBI Conserved Domain Database indicated CT263 might contain a provisional nucleosidase domain (PRK05634). To gain further support that CT263 could fulfill a role as a nucleosidase and complete the putative futalosine pathway within *Chlamydia*, *ab initio* modeling of CT263 was performed by the protein structure prediction platform I-TASSER (33–35). The highest ranked computational model of CT263 exhibited a *C*-score of 0.31, which indicates high confidence in model accuracy (*C*-score > -1.5 (36)). The top 10 structural analogs in the PDB of this model are all MTAN enzymes with r.m.s.d. values below 2.50 Å. As computational predictions for CT263 support a potential role as an MTAN enzyme, enzymatic studies using recombinant protein were initiated to further investigate these predictions.

Identification of CT263 Substrates and Hydrolyzed Products—MTAN enzymes have been demonstrated to hydrolyze a variety of substrates, including 5′-methylthioadenosine (MTA), AdoHcy, and 6-amino-6-deoxyfutalosine (AFL) (37–39). Typically, these enzymes catalyze *N*-glycosidic bond hydrolysis between N9 of adenine and C1 of the thioribose. Catalysis occurs upon protonation at N7 of the substrate, and the S_n1-like transition state is captured by a catalytic water (S_N) with loss of the *N*-ribosidic bond (N9–C1) and release of adenine (40–43). Effi-

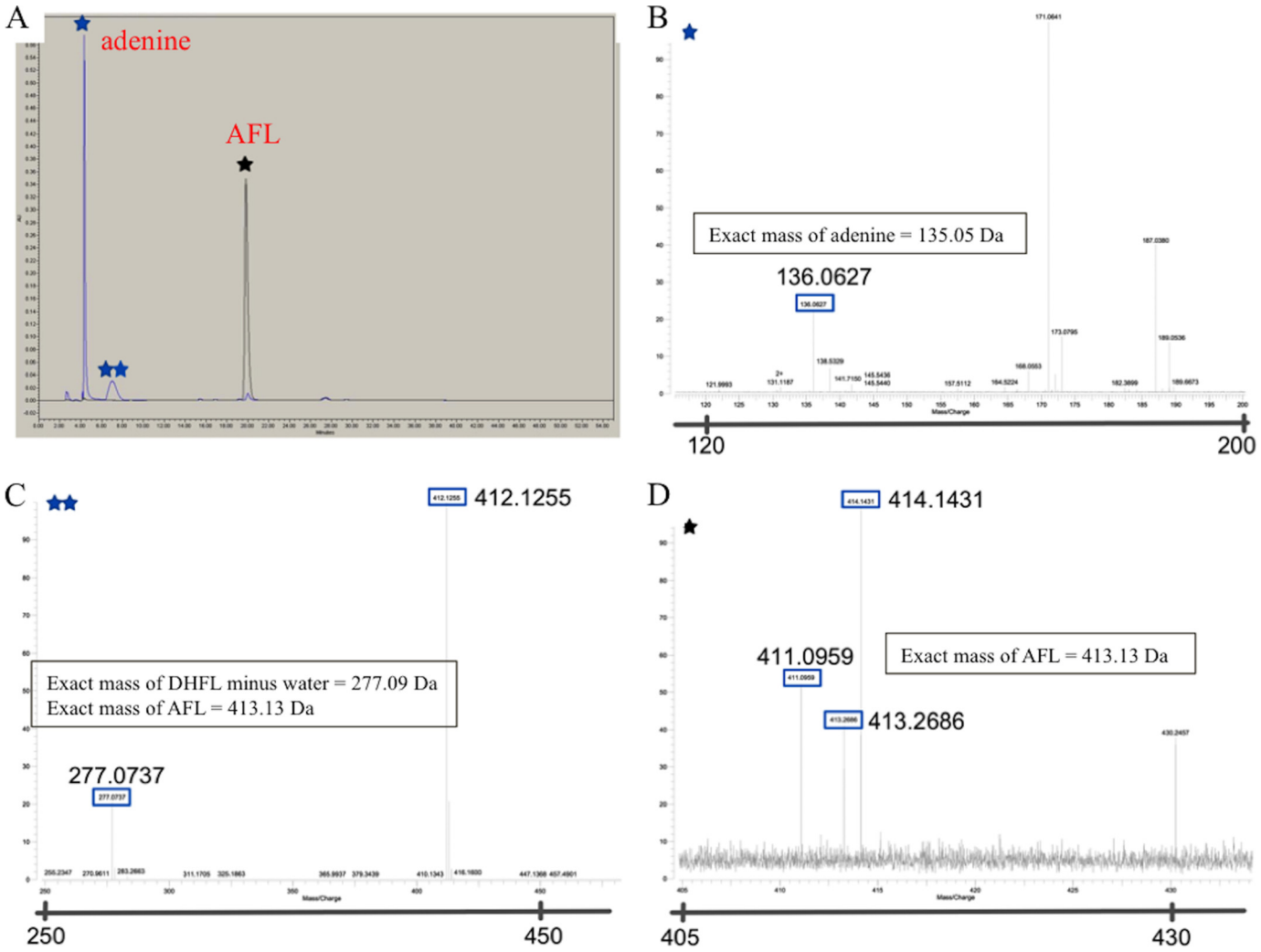

FIGURE 2. **Identification of CT263 substrates and hydrolyzed products.** *A,* HPLC reaction traces showing unreacted AFL (*black*) and the reaction products after addition of CT263 (*blue*). Reactions were initiated by the addition of CT263 (250 nM) and allowed to react overnight. *B–D,* mass spectrometry data for the *starred peaks* in *A*. The isolated peaks indicated by the corresponding *asterisk* were analyzed on a Varian 12T Fourier transform mass spectrometer in both positive and negative modes. *B,* spectra were obtained in negative mode. *Boxed peak* corresponds to the calculated mass of adenine. *C,* spectra were obtained in negative mode. *Boxed peaks* correspond to the calculated mass of DHFL minus water and AFL. *D,* spectra were obtained in positive mode. *Boxed peaks* correspond to the calculated mass of AFL.

cient processing of these substrates is critical for biochemical pathways involving the products of AdoMet utilization (44, 45). Accumulation of MTA is reported to cause feedback inhibition of polyamine biosynthesis (46, 47) and AdoMet-dependent methylation events, whereas AdoHcy hydrolysis provides precursors for biosynthesis of quorum-sensing compounds. Thus, proper MTAN function is essential to bacteria that require these pathways.

Purified recombinant CT263 was incubated with a variety of potential MTAN substrates, including AFL, AdoHcy, MTA, and ATP. HPLC analysis of the reaction mixtures post-CT263 addition revealed that only AFL resulted in substrate conversion (Fig. 2*A*). Reaction mixtures containing AdoHcy or MTA did not result in substrate conversion (data not shown), indicating that CT263 does not function as a canonical MTAN. The product peaks generated by HPLC were confirmed via Fourier transform mass spectrometry (Fig. 2, *B–D*) to be that of adenine and dehypoxanthinyl futalosine (DHFL). The observed mass of DHFL indicates that the water-bound intermediate was not observed and is likely unstable under these conditions. Catalysis of AFL to adenine and DHFL indicates that CT263 likely functions within the futalosine pathway (Fig. 1). However, the absence of MTA/AdoHcy hydrolytic activity suggests that in contrast to the bioinformatic predictions, CT263 does not function as a prototypical MTAN.

Kinetic Characterization of Wild-type C. trachomatis CT263—The ability of CT263 to hydrolyze AFL was further investigated under steady-state conditions (Fig. 3). The results of this assay reveal an apparent K_m of 8.3 ± 0.9 μM. The k_{cat} derived from fitting the curve to the equation for substrate inhibition is 0.91 ± 0.3 min^{-1}. Despite the relatively low catalytic efficiency (k_{cat}/K_m value of 1.8 × 10^3 M^{-1} s^{-1}), CT263 is competent for AFL hydrolysis. In the absence of strong selective pressure (*e.g.* synthesis of secondary metabolites), enzyme catalytic rates typically do not evolve toward maximal levels. The catalytic efficiency of an average enzyme is ~1 × 10^5 M^{-1} s^{-1}; however, enzymes that function within secondary metabolite pathways are, on average, ~30 times slower (48). Thus, the enzymatic rate

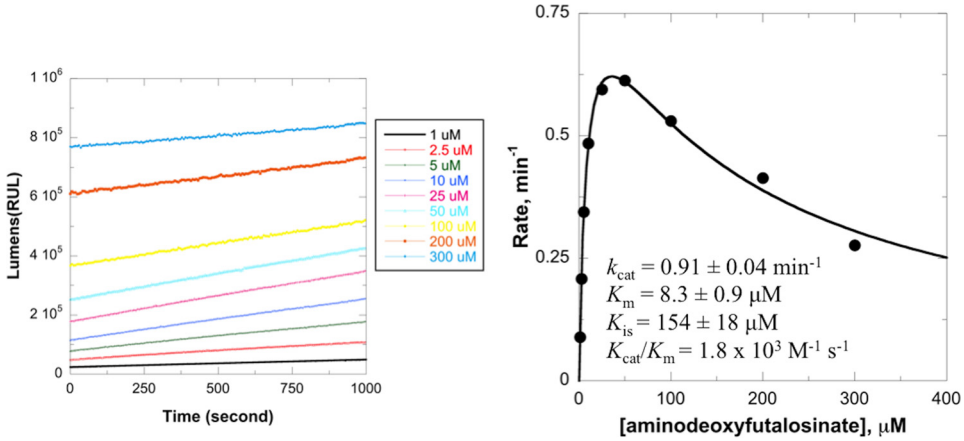

FIGURE 3. **Enzymatic characterization of CT263.** Initial rate (lumens/s) of catalytic activity with increasing concentrations of CT263 (*left panel*) and plotted as a function of increasing substrate (●, AFL) concentration (*right panel*). Rate kinetics (substrate k_{cat} and K_m and product K_{is}) were calculated by fitting to the Michaelis-Menten equation. Assay conditions (luciferase-based) are detailed under "Experimental Procedures."

TABLE 2

X-ray diffraction data and structure refinement

	CT263 native	CT263 fold	CT263 SeMet	CT263 adenine	CT263, D161N native	CT263 D161N MTA
PDBcode	4QAQ		4QFB	4QAR	4QAS	4QAT
Data collection						
Unit-cell parameters (Å)	a = 65.96, b = 104.5, c = 58.31	a = 65.24, b = 103.8, c = 57.92	a = 60.85, b = 74.23, c = 78.06	a = 65.64, b = 104.5, c = 58.21	a = 65.44, b = 104.2, c = 58.15	a = 65.88, b = 104.3, c = 58.22
Space group	$P2_12_12$	$P2_12_12$	$P2_122_1$	$P2_12_12$	$P2_12_12$	$P2_12_12$
Resolution (Å)[a]	55.77-1.58 (1.62-1.58)	43.31-2.60 (2.71-2.60)	47.99-1.99 (2.03-1.9)	65.64-1.45 (1.45-1.47)	104.15-1.25 (1.27-1.25)	104.26-1.75 (1.78-1.75)
Wavelength (Å)	1.0000	1.03969	0.97911	1.0000	1.0000	1.0000
Temperature (K)	100	100	100	100	100	100
Observed reflections	365,303 (17,639)	78,252 (9,308)	153,450 (10,199)	441,820 (19,724)	714,770 (33,502)	271,538 (15,179)
Unique reflections	56,011 (2,751)	12,572 (1,504)	24,951 (1,672)	71,123 (3,459)	110,407 (5,413)	41,202 (2,223)
$\langle I/\sigma(I)\rangle$[a]	14.8 (2.2)	17.2 (4.8)	14.5 (4.1)	15.7 (2.5)	14.5 (1.9)	13.5 (2.0)
Completeness (%)[a]	100.0 (100.0)	99.5 (99.4)	99.4 (95.3)	99.3 (99.5)	100.0 (99.9)	99.9 (99.9)
Multiplicity[a]	6.5 (6.4)	6.2 (6.2)	6.2 (6.1)	6.2 (5.7)	6.5 (6.2)	6.6 (6.8)
R_{merge} (%)[a,b]	6.0 (85.7)	6.3 (33.6)	7.5 (38.1)	7.6 (92.9)	5.3 (92.1)	8.0 (94.3)
R_{meas} (%)[a,c]	7.1 (102.0)	7.4 (40.2)	8.9 (45.8)	8.3 (102.8)	5.7 (100.5)	8.7 (102.0)
R_{pim} (%)[a,c]	3.8 (54.7)	3.9 (16.4)	4.8 (24.8)	3.4 (43.2)	2.2 (39.8)	3.4 (38.6)
$CC_{1/2}$[d]	99.9 (78.6)	99.7 (91.4)	99.7 (92.9)	98.6 (79.4)	99.9 (74.1)	99.9 (78.5)
Phasing						
Anom, completeness (%)[a]		96.7 (95.9)	92.8 (89.7)			
Anom. multiplicity[a]		3.2 (3.1)	2.9 (2.8)			
FOM		33.6	27.9			
Refinement						
Resolution (Å)	40.95-1.58		39.04-1.99	33.45-1.45	33.37-1.25	43.62-1.75
Reflections (working/test)	55,591 (2,840)		23,618 (1,880)	70,635 (3,573)	110,323 (5,516)	41,136 (2,069)
R_{factor}/R_{free} (%)[e]	16.56/19.87		16.65/2.16	18.69/21.68	17.76/19.54	16.56/19.57
No. of atoms (protein/ligand/solvent)	2,980/0/234		3,050/0/136	3,007/10/310	3,021/0/419	3,054/20/241
Model quality						
r.m.s.d.						
Bond lengths (Å)	0.009		0.012	0.010	0.009	0.010
Bond angles (°)	1.026		1.109	1.059	1.071	1.105
All-atom Clashscore	0.17		1.37	0.83	3.25	1.65
Average B-factor (Å^2)						
All Atoms	30.4		27.54	21.9	25.3	34.3
Protein	30.0		27.48	21.1	24.1	33.9
Ligand	NA		NA	31.4	NA	37.5
Solvent	36.4		28.79	29.6	34.6	38.6
Coordinate error, maximum likelihood (Å)	0.15		0.19	0.16	0.14	0.19
Ramachandran Plot						
Most favored (%)	97.9		96.3	97.9	97.3	97.9
Additionally allowed (%)	2.1		3.2	2.1	2.6	2.1
Outliers (%)	0.0		0.5	0.0	0.3	0.0

[a] Values in parentheses are for the highest resolution shell.

[b] $R_{merge} = \Sigma_{hkl}\Sigma_i|I_i(hkl) - \langle I(hkl)\rangle|/\Sigma_{hkl}\Sigma_i I_i(hkl)$, where $I_i(hkl)$ is the intensity measured for the ith reflection and $\langle I(hkl)\rangle$ is the average intensity of all reflections with indices hkl.

[c] R_{meas} = redundancy-independent (multiplicity-weighted) R_{merge} (15, 66). R_{pim} = precision-indicating (multiplicity-weighted) R_{merge} (67, 68).

[d] $CC_{1/2}$ is the correlation coefficient of the mean intensities between two random half-sets of data (65, 69).

[e] $R_{factor} = \Sigma_{hkl}||F_{obs}(hkl)| - |F_{calc}(hkl)||/\Sigma_{hkl}|F_{obs}(hkl)|$; R_{free} is calculated in an identical manner using 5% of randomly selected reflections that were not included in the refinement (SeMet-CT263 = 8%).

of CT263 is actually in line with the average rate of previously characterized secondary metabolite enzymes.

The catalytic efficiency of MqnB/MTAN enzymes with broader specificity, including both MTA and AFL, is greater. The MTANs from *Campylobacter jejuni* and *Helicobacter pylori* were reported to give k_{cat}/K_m values of 5.3×10^5 and 5.4×10^6 M^{-1} s^{-1}, respectively (47, 50). Although the k_{cat} value of CT263 is similar, its K_m value is complicated by substrate inhibition, where larger concentrations of AFL inhibit catalysis, with a dissociation constant of 154 μM (Fig. 3). It is important to note that enzymes within bacterial vitamin/cofactor pathways typically exhibit modest catalytic capacity. For example, the

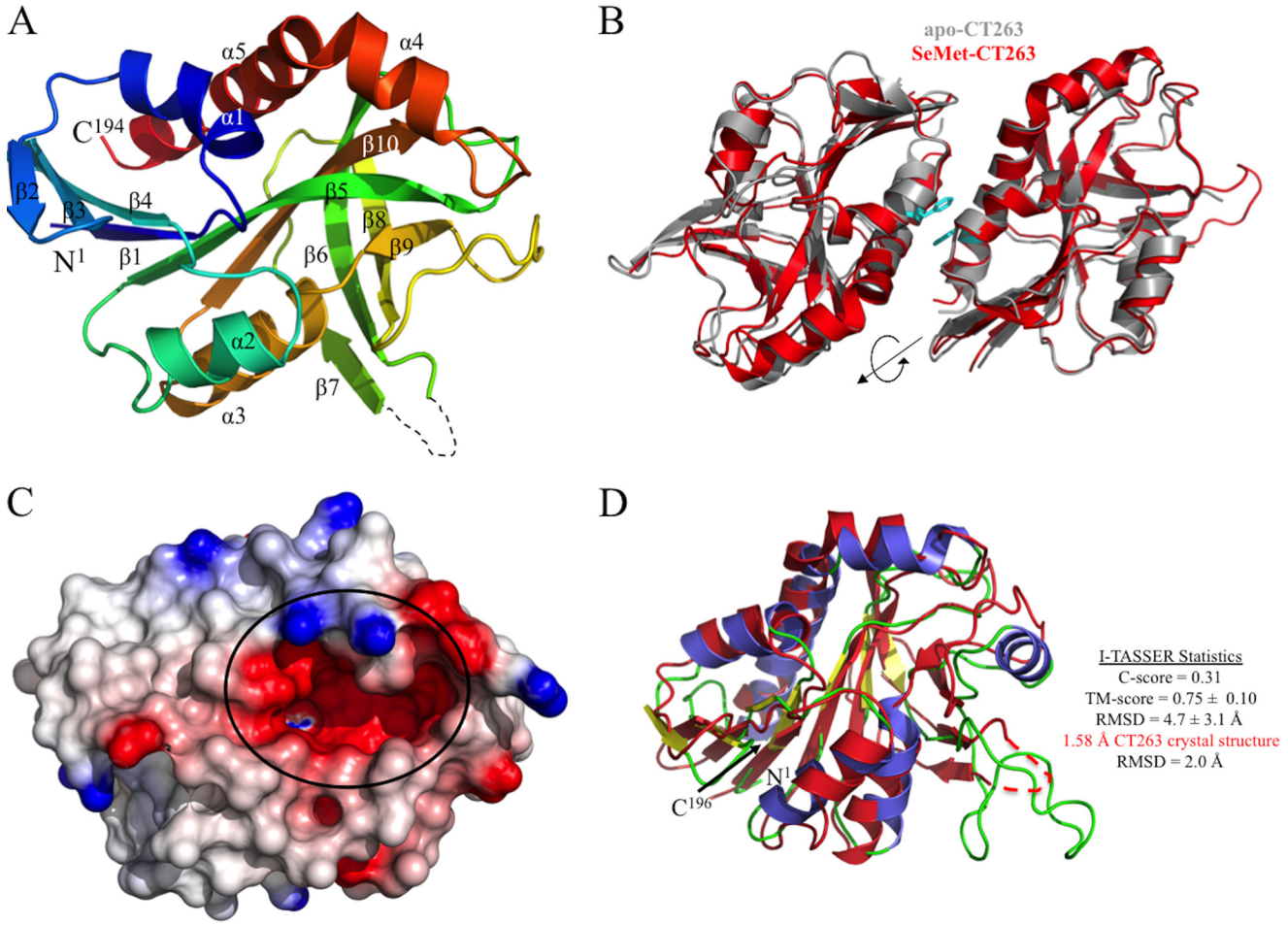

FIGURE 4. **Crystal structure (1.58 Å) of CT263 from *C. trachomatis*.** *A,* crystal structure of CT263 is shown in cartoon ribbon format using common rainbow colors (slowly changing from *blue* N terminus to *red* C terminus). Secondary structure lacking interpretable electron density is shown as *dashed line*. *B,* structural superposition of CT263 dimers from $P2_12_12$ (apo- and ligand-bound) and $P2_122_1$ (SeMet) crystals shown in cartoon ribbon format. Wild-type CT263 dimer (*gray*) is generated by applying the symmetry operator $(-x+2,-y,z)$, although the SeMet-CT263 dimer (*red*) is found within the asymmetric unit. Phe-187 side chains (*cyan, balls-and-sticks*) participating in π-π bonding and highlight the 2-fold symmetry within this interface. *C,* surface representation of electrostatic potential, generated by DelPhi (28), of CT263 (same orientation as *A*). Color scheme represents regions of negative (*red*) and positive (*blue*) charge density contoured at ± 5 *e*/*kT*. Putative active site cleft is highlighted by a *black circle*. *D,* structural superposition of I-TASSER (33–35) computational model depicted in cartoon ribbon format (*blue,* α-helices; *yellow,* β-sheets; random coil, *green*) and 1.58 Å crystal structure of CT263 (cartoon ribbon format, colored *red*). Two structures align with an r.m.s.d. of 2.0 Å across all Cα atoms.

synthesis of an electron carrier within *Actinomycetes* has a reported k_{cat}/K_m of 2.0 M^{-1} s^{-1} (49), roughly 900 times less efficient than CT263. To further understand the enzymatic properties of CT263, recombinant protein was entered into crystallization trials so that the catalytic site could be structurally investigated.

1.58 Å Crystal Structure of CT263 from C. trachomatis—Orthorhombic crystals ($P2_12_12$) of CT263 were grown, and the structure was determined by Au-SAD (all molecular replacement phasing attempts with homology models were unsuccessful) and refined against native x-ray diffraction data to a resolution of 1.58 Å (Table 2). CT263 is composed of a single globular domain (Fig. 4*A*) with dimensions ~30 × 30 × 45 Å. The mixed α/β fold of CT263 consists of a central core of 10 twisted β-sheets flanked by two sets of paired α-helices with the following topology: β1-α1-β2-β3-β4-α2-β5-β6-β7-β8-β9-α3-β10-α4-α5. Two polypeptides were found within the asymmetric unit. Numbering of all residues in this work reflects their position in the *C. trachomatis* CT263 sequence.

In contrast to all other CT263 structures presented herein, selenomethionine-labeled CT263 crystallized in a different orthorhombic space group ($P2_122_1$). Structural superposition of both experimentally determined CT263 protomers indicates that they are highly similar to each other, with an r.m.s.d. of 0.29 Å across all Cα atoms. Additionally, two polypeptides are also found within the asymmetric unit (Fig. 4*B*).

Consistent with a potential enzymatic function, the CT263 structure contains a large, surface-exposed cleft (*black circle* in Fig. 4*C*) predominantly formed by α2, α4, and the loop connecting β8-β9. Additionally, the putative active site cleft of CT263 is characterized by a high degree of electronegative charge density (Fig. 4*C*). This striking feature likely reflects an important contribution to substrate binding. Structural superposition of the computational I-TASSER model and x-ray crystal structure of CT263 (Fig. 4*D*) validates the high confidence of the *ab initio* modeling process with an impressive r.m.s.d. of 2.0 Å across all Cα atoms. Although the core fold of each structure is highly similar, modeled loop regions in the I-TASSER struc-

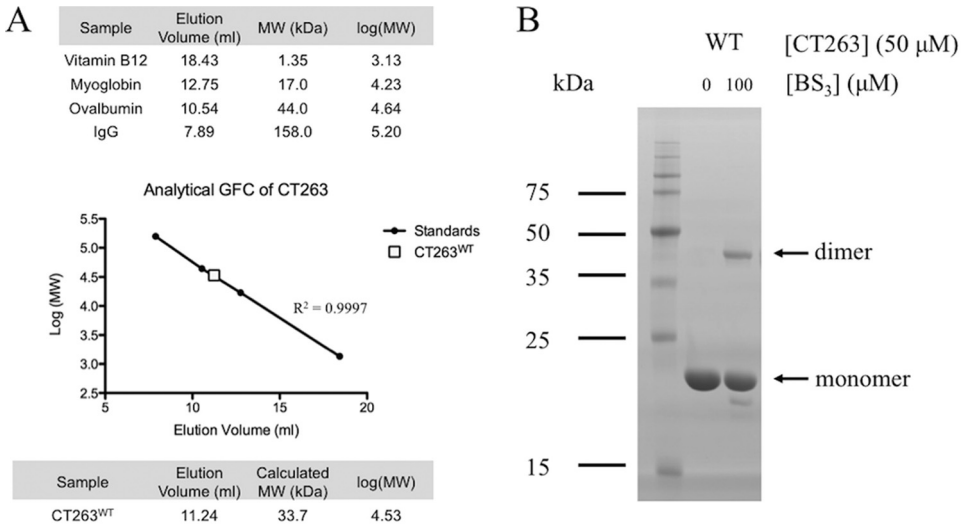

FIGURE 5. **Analysis of the CT263 quaternary structure in solution.** *A,* purified CT263 was injected onto an analytical gel filtration column (Superdex 75 10/300 GL, GE Healthcare), and the elution profile (*bottom table*) was compared with a series of known standards (*top table*; Bio-Rad) to derive an estimation of protein molecular weight. The standards are shown as *black circles* (log M_r *versus* elution volume plot, $R^2 = 0.9997$), and CT263 is represented as a *white square*. *B,* purified CT263 (50 μM) was incubated with the amine-reactive cross-linking agent BS^3 (100 μM) at room temperature for 60 min, quenched with 100 mM Tris-HCl (pH 7.5), and analyzed by SDS-PAGE. Apparent M_r of CT263 monomer and dimer indicated by *black arrows*. *1st lane* contains protein ladder.

ture are quite different. These model errors likely account for the unsuccessful use of the I-TASSER model in molecular replacement and could potentially reflect the altered enzymatic profile of CT263.

Oligomeric State of CT263 in Solution—As two polypeptides were found within both CT263 and SeMet-CT263 asymmetric units, the protein interfaces and assemblies (PISA) server (28) was used to assess potential modes of oligomerization. The most thermodynamically favorable assembly was predicted to be a dimer; however, PISA analysis indicated multiple potential interfaces could be adopted within either crystal system. Intriguingly, only one interface is found within both structures (Fig. 4*B*), suggesting it could be physiologically relevant. This interface buries ~536 Å^2 (6% of the available surface area) with a predicted ΔG of −4.1 kcal/mol and exhibits 2-fold crystallographic symmetry (operator: $-x + 2, -y, z$). Several side chains from each protomer are within hydrogen bonding distance (2.5–3.4 Å) and, along with numerous hydrophobic contacts, stabilize the interface. These interactions include Arg-16–Ser-19, Gln-180–Leu-20, Tyr-190–Glu-184, and Tyr-22–Glu-184. Additionally, the side chains of Phe-187 from each protomer participate in π-π bonding (Fig. 4*B*). To provide support for this dimer, the oligomeric state of CT263 was further analyzed in solution.

Analytical gel filtration chromatography was used to investigate the oligomeric state of CT263 in solution (Fig. 5*A*), which indicated that wild-type CT263 eluted as a single tailed peak with an apparent molecular mass of 33.7 kDa. This value is much larger than would be expected for monomeric CT263 (~22 kDa), yet smaller than for a dimer (~44 kDa). Reversible association in solution is a common phenomenon with protein oligomeric assemblies. Previous analysis of the effects of reversible dimerization during gel filtration chromatography provides insight into the CT263 chromatogram (50). A tailed peak with a retention time in between those of monomer and dimer suggests fast dimer association and dissociation, supporting the potential for CT263 to dimerize.

TABLE 3
CT263 DALI search statistics

CT263 structural homology, top 5 (unique) DALI scores					
Protein name	PDB code	Z-score[a]	r.m.s.d.	Cα range[b]	% ID[c]
MTAN, *H. pylori*	4BMZ	22.3	2.2	189/230	16
MTAN, *A. thaliana*	2H8G	21.6	2.4	191/246	17
MTAN, *F. philomiragia*	4JOS	21.5	2.3	188/230	13
MTAN, *S. denitrificans*	4JWT	21.4	2.4	191/245	14
MTAN, *S. aureus*	3BL6	20.9	2.4	186/230	16

[a] Similarity score representing a function that evaluates the overall level of similarity between the two structures. *Z*-scores higher than 8.0 indicate that the two structures are most likely homologous (51).
[b] Data denote the number of residues from the query structure that superimpose within an explicit distance cutoff of an equivalent position in the aligned structure.
[c] Data denote the percent sequence identity across the region of structural homology.

As analytical gel filtration chromatography analysis of CT263 did not conclusively indicate a dimeric state was adopted in solution, the chemical cross-linker BS^3 (amine-to-amine, 11.4 Å spacer length) was utilized to probe for the formation of higher order complexes (Fig. 5*B*). Incubation of CT263 (50 μM) with 100 μM BS^3 leads to the formation of a single higher order band of the approximate molecular weight for a CT263 dimer. Increasing concentrations of BS^3 failed to produce any higher molecular weight bands (data not shown). Altogether, these observations provide support that the symmetric CT263 dimer likely exists in solution.

Structural Similarities Suggest CT263 Is an MTAN—The PDB was queried with the protein structure homology server DALI (51) to identify functionally characterized proteins that are structurally similar to CT263. The top five scoring unique hits are listed in Table 3. Each of these structures, as well as the next ~50 hits, is an MTAN enzyme. Each of these structures aligns to CT263 with an r.m.s.d. of 2.50 Å or lower, and the overall topology of CT263 is consistent with the consensus

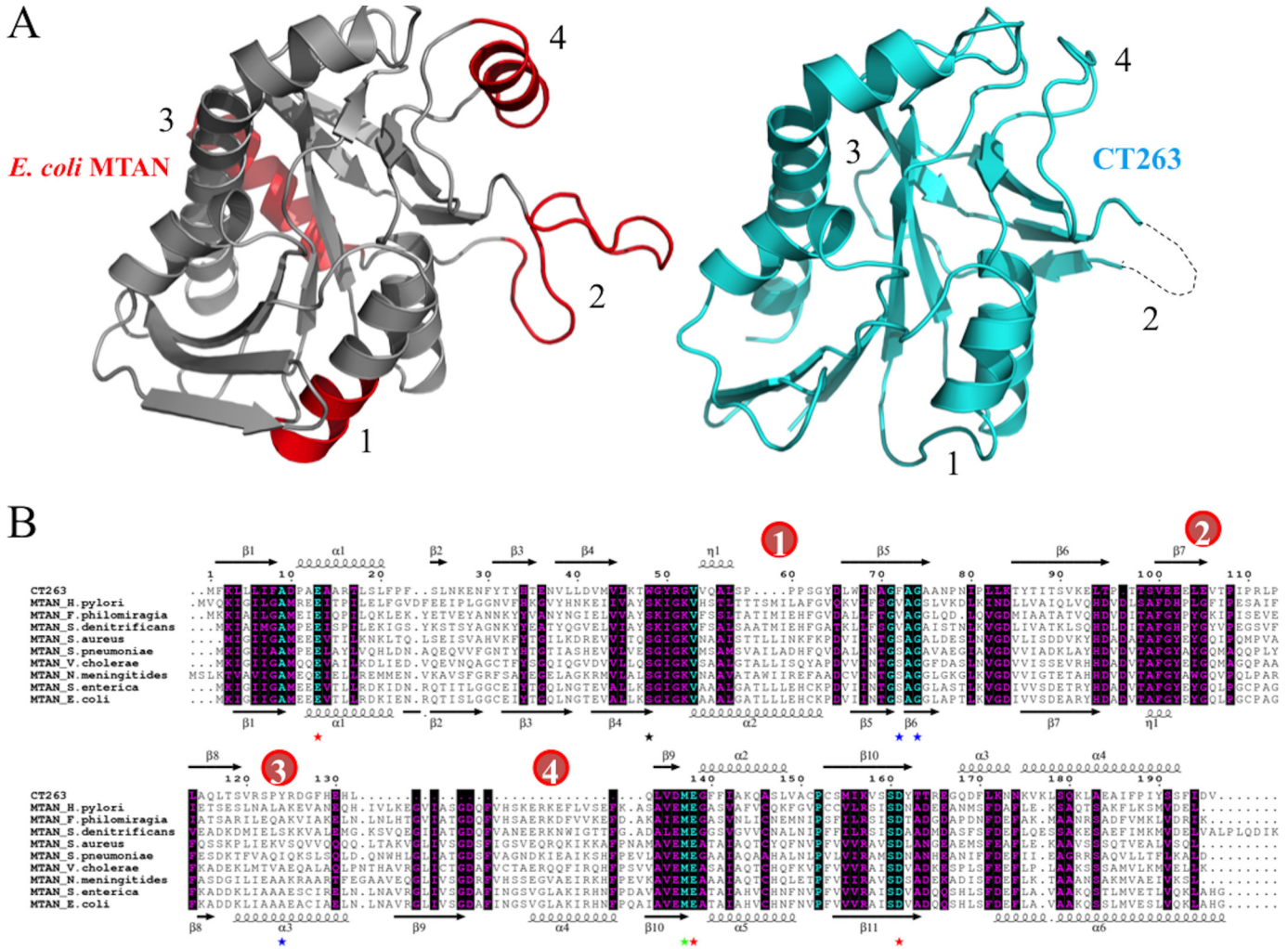

FIGURE 6. **Structure and sequence conservation of CT263 and MTAN members.** *A,* structural superposition of *E. coli* MTAN (PDB code: 1Z5P, *gray*) and CT263 (*cyan*) structures depicted in cartoon ribbon format and translated apart for clarity. Several regions of structural difference are highlighted in *red* (*E. coli* MTAN) and numbered on each structure. Secondary structure lacking interpretable electron density within CT263 is shown as *dashed line* (residues 96–101). *B,* limited structure-based alignment of CT263 and MTAN members from the DALI search (Table 3) (51) was generated using ClustalW (23) and rendered with ESPRIPT (24). The *numbers* above the sequences correspond to *C. trachomatis* CT263. The secondary structure of CT263 is shown above the alignment, and the secondary structure of *E. coli* MTAN (PDB code: 1Z5P) is shown below. Numbered regions correspond to structural differences highlighted in *A*. Residues are colored according to conservation (*cyan,* identical, and *purple,* similar) as judged by the BLOSUM62 matrix. *Red stars* below the sequences correspond to catalytic triad amino acid side chains; *blue stars* correspond to adenine-bound side chains, and *green stars* correspond to ribosyl-bound side chains in the CT263^{D161N}-MTA structure; and the *black star* corresponds to the active site CT263 side chain that is disordered in the absence of ligand. Accession numbers are detailed under "Experimental Procedures."

MTAN fold (Fig. 6*A*). These observations are consistent with the high degree of structural similarity between the CT263 computational model and crystal structures.

There are several notable structural differences between CT263 and the queried MTANs (*four regions highlighted* in Fig. 6) that could potentially account for the altered enzymatic profile of CT263. Helix α2 typically involves at least four turns in prototypical MTANs, yet only completes two turns within CT263 (*region 1* in Fig. 6*A*). Perhaps the most pronounced structural difference within CT263 is found within the loop region connecting β6-β7 (*region 2* in Fig. 6*A*). This region is typically involved in dimerization (Fig. 7), where it contributes side chains involved in active site interactions within all structurally characterized MTANs (41, 52–58). The absence of this region reflects the altered CT263 dimer assemblies relative to the prototypical MTAN dimer interface. Within canonical MTANs, the loop connecting β7-β8 is typically α-helical (*region 3* in Fig. 6*A*; α3 in *E. coli* MTAN in Fig. 6*B*); however, this region is composed of a random coil in CT263. The role of α3 in prototypical MTAN functionality is currently unclear. Finally, region 4 of CT263 also adopts a random coil conformation instead of α-helical structure. This region is involved in the canonical MTAN dimer interface. Despite these numerous peripheral structural differences, the core fold of CT263 clearly resembles prototypical MTANs.

The high degree of structural conservation between CT263 and prototypical MTANs is remarkable given the absence of significant sequence level homologs to CT263. Multiple sequence alignment of CT263 with the most structurally similar MTANs (Fig. 6*B*) identified by DALI (highest sequence identity: *A. thaliana* MTAN, 17%; Table 3) provides a plausible explanation for the absence of the canonicalMTAN dimer interface. CT263 is composed of 196amino acids, and the shortest MTAN analyzed in this study (*S. aureus*, PDB code 3BL6)

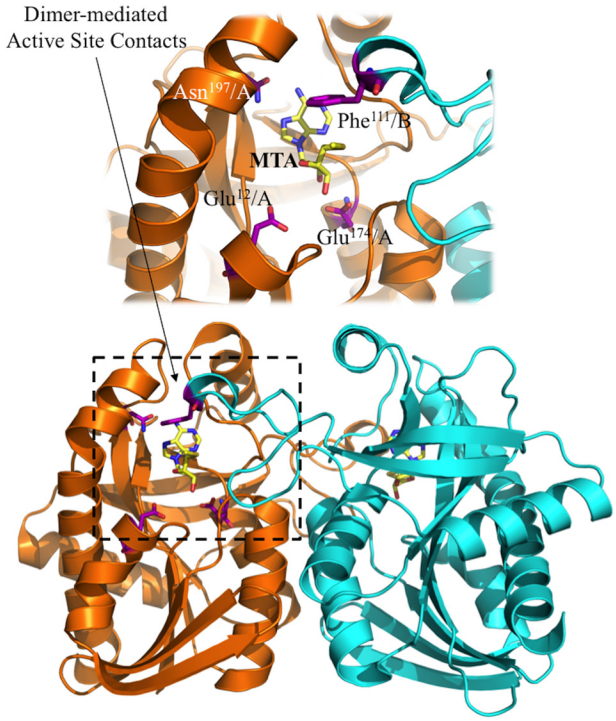

FIGURE 7. **Dimer-mediated contacts within prototypical MTANs.** Physiologic dimer of MTA-bound *E. coli* MTAN (PDB code: 1Z5O) shown in cartoon ribbon format. Each protomer is individually colored (*orange* and *cyan*). MTA molecule (*balls-and-sticks, yellow*) modeled in each active site. Catalytic triad and dimer-mediated aromatic residues are shown as *balls-and-sticks* and colored *purple*. *Inset*, *dashed box* indicates magnified active site region.

was composed of 228 amino acids.Multiple sequence alignment indicates that the majority of thisdifference is localized to a single contiguous stretch of CT263(primarily involving *regions 2* and *4* in Fig. 6). Additionally, theresidues that are present within region 3 are in poor sequence-level agreement with the queried MTAN structures.

Even though the prototypical MTAN dimer interface is absent within CT263, the amino acids that are highly conserved cluster within the surface-exposed cleft of CT263 (Fig. 8*A*), as determined by the evolutionary conservation server Consurf (29). Furthermore, the extensively studied catalytic triad of carboxylic acid side chains that are critical for enzymatic MTAN function (41) are conserved in CT263 (*red stars* in Fig. 6*B*) and located within the putative active site cleft. Accordingly, the structural similarities between CT263 and canonical MTANs clearly support the observed nucleosidase activity. In addition, the significant structural differences also provide a plausible explanation for the absence of MTA/AdoHcy hydrolytic activity because of the absence of dimer-mediated active site interface.

Structural Insights into the CT263 Active Site through Substrate and Product Binding—To further investigate the function of CT263 and the nature of substrate binding, AFL was incubated with CT263 prior to crystallization. However, upon inspection of the resulting electron density maps, no unaccounted for density was visible within the putative active sites (data not shown). Thus, in light of the apparent inability of CT263 to efficiently hydrolyze MTA (*substrate image in* Fig. 8*B*), we hypothesized that this compound could be utilized to further investigate the function of CT263 with respect to the nature of substrate binding. Wild-type CT263 was incubated with MTA prior to crystallization, and the resulting crystals diffracted x-rays to 1.45 Å (Table 2). A single region of unaccounted for electron density was visible up to 5.0 σ within only one active site cleft (Fig. 8*C*) of the asymmetric unit dimer. However, it appears that the incubated substrate was actually hydrolyzed by the crystallized enzyme, as the electron density perfectly accommodated an ADE molecule (complex termed WT-ADE, Fig. 9*A*). The same protein sample of wild-type CT263 was used in all crystallization trials, suggesting the adenine molecule was not an artifact of co-purification, a common occurrence in MTAN crystal structures (54, 58). Given the kinetic characterization of CT263, MTA hydrolysis was rather unexpected; however, it is noteworthy that the time scale of crystallization was significantly longer than the enzymatic assay (18 h incubation with 250 nM of CT263). This specific catalytic functionality is therefore not likely to be biologically relevant.

Numerous protein contacts are within hydrogen bonding distance of adenine (Fig. 9*A* and Table 4), including the side chain of the catalytic triad residue Asp-161, main chain atoms from Phe-72 and Gly-74 that are found within a highly conserved region of prototypical MTANs (*blue stars* in Fig. 6*B*), and main chain atoms from Tyr-124. The WT-ADE structure is almost identical to the apo-CT263 structure, with an r.m.s.d. of 0.50 Å across all residues. However, the loop connecting β8 and β9 has shifted ~1.5 Å toward the substrate, and two side chains (Arg-125 and Gln-168) near the bound adenine have reoriented (*middle panel* in Fig. 9*B*), further constricting the active site cleft and reducing solvent exposure to the bound product.

In pursuit of a nonhydrolyzed enzyme-substrate complex, Asp-161 was mutated to Asn ($CT263^{D161N}$), a substitution that has previously proven adventitious in obtaining enzyme-substrate complexes (41, 57). $CT263^{D161N}$ was expressed, purified, and crystallized in essentially the same manner as wild-type CT263. The structure of apo-$CT263^{D161N}$ was determined to 1.27 Å (Table 2) and shares near-identity with wild-type CT263 giving an r.m.s.d. of 0.28 Å across all residues. MTA was incubated with mutant $CT263^{D161N}$ prior to crystallization, and the resulting crystals diffracted x-rays to 1.75 Å (Table 2). In contrast to wild-type enzyme, the substrate appeared to be intact as a larger region of contiguous electron density was again apparent within only a single active site of the $CT263^{D161N}$ asymmetric unit dimer (Fig. 8*D*). Unexpectedly, the mutant-substrate complex (termed $CT263^{D161N}$-MTA) remained in a nearly identical structural conformation as ADE-bound wild-type CT263, as judged by structural alignment (r.m.s.d. values of 0.35 Å across all residues). The same residues that reoriented in the WT-ADE structure are in identical positions in the $CT263^{D161N}$-MTA structure. Additionally, interactions with the purine base of MTA are equivalent to those described in the WT-ADE complex. Importantly, the bonding distances between mutant Asn-161 and bound ligand (2.6 Å/N7 and 2.9 Å/N6 for WT-ADE and 3.1 Å/N7 and 3.1 Å/N6 for $CT263^{D161N}$-MTA) are much longer in the mutant complex, indicating proton donation to N7 of the adenine moiety is likely significantly reduced by this substitution.

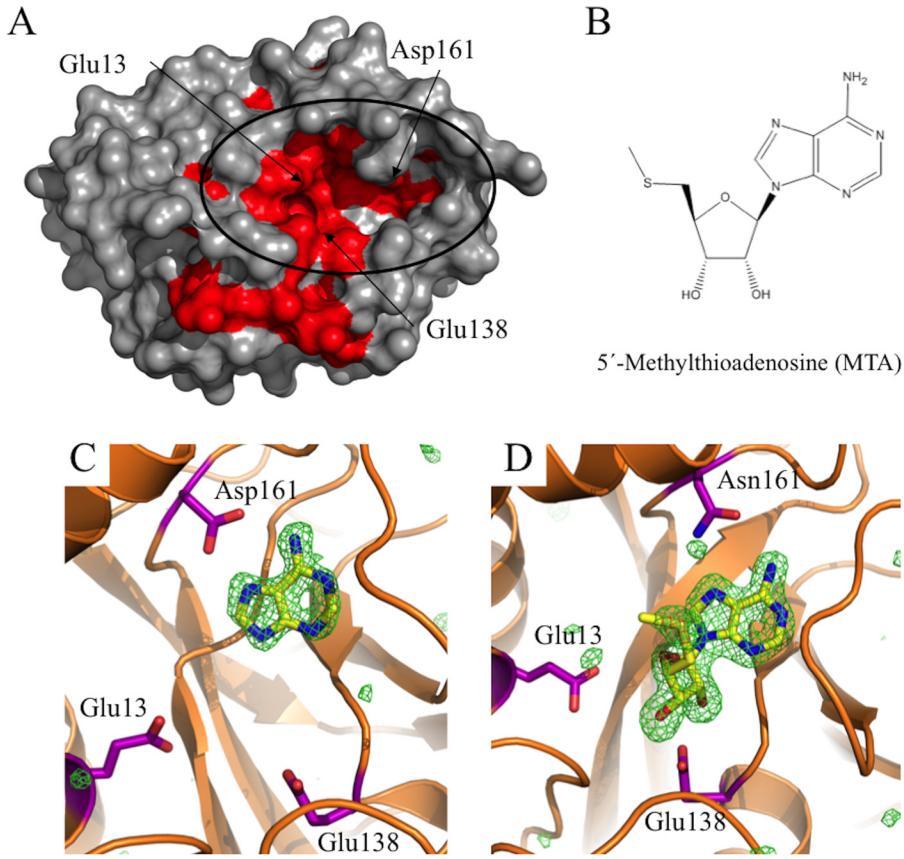

FIGURE 8. **Structural insights into CT263 active site.** *A,* conservation plot of surface-exposed CT263 amino acid side chains, as generated by CONSURF (29). Color scheme depicts strongly conserved side chains in *red*. Putative active site cleft is highlighted by *black circle* and catalytic triad residues are labeled (*red stars* in Fig. 6*B*). *B,* $F_o - F_c$ map (*green mesh* at 4.0 σ contour) of the fully refined CT263^{WT}-ADE structure in the absence of modeled ligands (ADE shown for clarity). Catalytic triad side chains are depicted as *balls-and-sticks* (*purple*). Backbone is depicted in cartoon ribbon format (*orange*). *C,* MTA. *D,* $F_o - F_c$ map (*green mesh* at 4.0 σ contour) of the fully refined CT263^{D161N}-MTA structure in the absence of modeled ligands (MTA shown for clarity). Coloring is the same as *B*.

Protein contacts with the MTA sugar moiety (Fig. 9*C,* Table 4, and *green star* in Fig. 6*B*) involve hydrogen bonding interactions between the ribosyl 2′- and 3′-hydroxyls and both Glu-138 oxygen atoms as well as the main chain nitrogen of Met-137 (an invariant MTAN residue). The nucleoside region of MTA adopts a C4′-*endo* sugar pucker and a *syn* ribosidic bond, indicative of a high energy conformation. Identification of the catalytic water is slightly confounded by the presence of four waters at the base of the active site cleft (*red spheres* in Fig. 9*C*). The presence of a "water-wire" channel for the catalytic nucleophile was previously observed in *S. enterica* MTAN (*Se*MTAN (54)). Within the CT263^{D161N}-MTA structure, only one of these four waters is within appropriate bonding distance of the catalytic triad residue Glu-13 (2.6 Å) and C1 (3.6 Å) of MTA (*large red sphere* in Fig. 9*C*), indicating this water is the most likely S_N candidate.

The 5′-alkylthio side chain of MTA lacks any noticeable hydrogen bonding interactions with CT263^{D161N}; however, the side chain of Trp-48 forms a hydrophobic barrier parallel to this region of MTA (Fig. 9*C*; distance of ~3.8 Å at each atom). Intriguingly, side chain density for Trp-48 was disordered in all previously discussed structures (including SeMet-CT263). This indicates that the presence of MTA increases protein order within CT263. Active site stabilization in CT263 gives some insight into the potentially unique mechanism of CT263-substrate binding, as this aromatic residue is absent from prototypical MTANs (*black star* in Fig. 6*B*). Typically, MTANs encode an aromatic side chain (Phe/Tyr) on a loop from the second monomer, which occludes the active site of the first monomer upon substrate binding (Fig. 7). In *Se*MTAN, the 5′-alkylthio side chain of the transition state inhibitor MT-DADMe-ImmA was not within hydrogen bonding distance of this aromatic residue (Tyr-107); instead, extension of the 5′-alkylthio side chain by three carbons placed the ligand within hydrogen bonding distance of this residue (54). Providing further support for a unique role in substrate binding, Trp-48 is conserved throughout all chlamydial orthologs of CT263 (*red star* in Fig. 10). Altogether, these observations suggest that Trp-48 could potentially account for the lack of dimer-mediated contacts at the 5′-alkylthio-binding site within CT263.

Structural Comparison with SeMTAN Reveals That CT263 Is in the Closed Form—MTANs have been extensively studied from a structure/function standpoint in a variety of medically relevant pathogens, including *E. coli* (41, 56, 58), *H. pylori* (52, 53, 57, 59), *S. aureus* (60), and *S. enterica* (54), among others. All of these structures have crystallized with a conserved dimer interface (Fig. 7), involving a region that is absent within CT263 (*regions 2* and *4* within Fig. 6). The absence of this interface within CT263 resulted in the potential presence of novel dimeric contacts (Fig. 4*B*). The presence of a single occupied active site in substrate-bound complexes, as described within the ligand-bound CT263 structures, is quite common in proto-

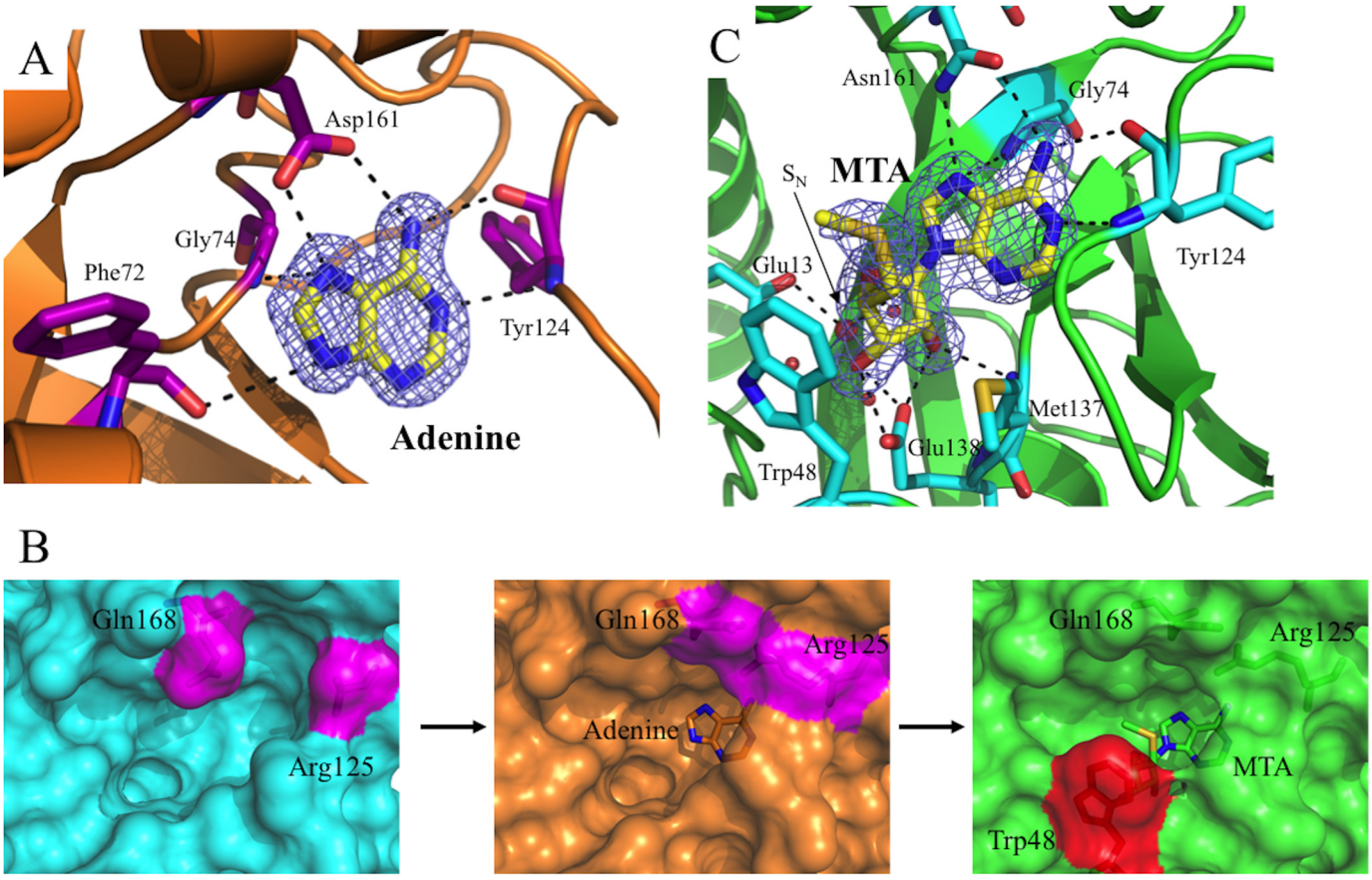

FIGURE 9. **Ligand-bound crystal structures of CT263.** *A*, $2F_o - F_c$ map (*blue mesh* at 1.0 σ contour) of the refined $CT263^{WT}$-ADE structure with one adenine molecule (*balls-and-sticks, yellow*) modeled in the active site. Active site side chains within hydrogen bonding distance (2.5–3.5 Å) of adenine are depicted as *balls-and-sticks* (*purple*), and CT263 backbone is depicted in cartoon ribbon format (*orange*). Further information on these distances can be found in Table 4. *B*, surface representation of CT263 structures depicting structural changes that occur upon binding ADE (*orange surface*) or MTA (*green surface*). Side chain residues for Arg-125 and Gln-168 reorient upon ligand binding (*solid circle*). Ordered electron density for Trp-48 (*dashed circle*) is only seen within MTA-bound structure (*green*). *C*, $2F_o - F_c$ map (*blue mesh* at 1.0 σ contour) of the refined $CT263^{D161N}$-MTA structure with one MTA molecule (*balls-and-sticks, yellow*) modeled in the active site. Active site side chains within hydrogen bonding distance (2.5–3.5 Å) of MTA are depicted as *balls-and-sticks* (*cyan*), and $CT263^{D161N}$ backbone is depicted in cartoon ribbon format (*green*). Further information on these distances can be found in Table 4. Putative catalytic water is shown as a *sphere* (*red*).

typical MTANs (52, 54, 59). The recent structure of ligand-bound *Se*MTAN highlights this effect, where one monomer was in the "closed" form, and the other remained empty and in the "open" form (54). Structural superposition of both open and closed *Se*MTAN monomers and the substrate-bound $CT263^{D161N}$-MTA monomer (Fig. 11) indicates that CT263 is in a similar conformation as ligand-bound *Se*MTAN (r.m.s.d. of 1.90 and 2.05 Å for closed and open conformations, respectively), particularly within the active site cleft (*boxed region* in Fig. 11). As the $CT263^{WT}$ and $CT263^{D161N}$-MTA structures adopted highly similar conformations, these observations suggest that CT263 is constitutively found in a closed-form conformation that is the substrate binding competent.

Molecular Modeling of 6-Amino-6-deoxyfutalosine Binding—Despite the fact that MTA was hydrolyzed within wild-type CT263 crystals, enzymatic analysis of CT263 indicates a preference for the futalosine pathway intermediate (Fig. 1), AFL. Efforts to co-crystallize $CT263^{D161N}$ with AFL failed to reveal novel regions of electron density in either active site cleft. However, given that the adenosyl moiety is structurally conserved across MTA, AdoHcy, and AFL, the $CT263^{D161N}$-MTA complex was used to model the binding location of AFL within the CT263 active site cleft (Fig. 12). As the structure of CT263 appears to represent a closed form conformation, residues contributing to binding of the aromatic isophthalic acid group of AFL are likely close to their current position. The only residue within this region capable of π-π bonding with the benzene ring of AFL is Trp-48, the position of which is supported by the CT263-AFL model and D161N-MTA complex. Additional binding specificity could originate from Lys-172 and Lys-175 (found on either side of the α4-α5 kink), which are appropriately positioned to interact with the carboxylic acid moiety of AFL. Further studies exploring AFL binding could provide insights into the development of specific transition-state inhibitors and anti-chlamydial compounds.

DISCUSSION

In order for a functional electron transport chain to assemble within Chlamydiaceae, lipid-soluble electron carriers (*e.g.* quinones) must be present. The potential source of quinones within Chlamydiaceae has yet to be established, with early speculation that they were scavenged from the host (10). However, the presence of a host scavenging translocator or complete quinone biosynthetic pathway was not

TABLE 4
CT263-ligand hydrogen bonding information

Enzyme		Ligand		
wild-type		Adenine (ADE)		
Amino Acid	Atom	Distance (Å)	Atom	Group
Tyr124	N	3.2	N1	
Tyr124	O	3.2	N6	
Asp161	OD2	2.9	N6	
Asp161	OD2	3.4	N7	
Asp161	OD1	2.6	N7	
Phe72	O	3.5	N9	
Gly74	N	3.3	N7	
D161N		MTA		
Gly74	N	3.5	N7	Adenine
Tyr124	N	3	N1	Adenine
Tyr124	O	3.2	N6	Adenine
Met137	N	2.8	O2'	2' Ribosyl
Glu138	OE1	3.2	O3'	3' Ribosyl
Glu138	OE2	2.7	O3'	3' Ribosyl
Glu138	OE1	3.4	O2'	2' Ribosyl
Asn161	OD1	3.1	N6	Adenine
Asn161	ND2	3.1	N7	Adenine

revealed upon genomic sequencing. Here, we provide the first experimental evidence that Chlamydiaceae can synthesize MK through the futalosine route, for potential use during oxidative cellular respiration.

Although the crystal structure of CT263 displays a high level of structural similarity with MTANs (Fig. 6*A*), the enzymatic characterization of CT263 indicates that only AFL can be hydrolyzed at a physiological rate. Traditionally, MTANs hydrolyze intermediates of AdoMet utilization pathways (37–39), which include substrates that were not processed by CT263 (*e.g.* MTA and AdoHcy, Fig. 9, *B* and *C*). Chlamydiaceae lack the apparent homologs necessary to process the products of MTAN-cleaved MTA and/or AdoHcy (10); however, the presence of a conserved AdoMet/AdoHcy antiporter (31) potentially alleviates the need for CT263 to deal with these metabolites and could account for the apparent lack of this enzymatic function.

We have provided structural evidence that CT263 adopts a novel dimer interface (Fig. 4*B*) compared with prototypical MTANs and that a single indel (*region 2* within Fig. 6*B*) is responsible for the missing region. Typically, upon substrate binding the MTAN active site is stabilized by both polypeptides of the dimer, with the residues responsible for interaction with the 5′-alkylthio moiety (*dashed box* in Fig. 7) coming from the region absent in CT263. Conversely, as the presented ligand-bound CT263 structures reveal, the nucleoside-binding pocket is highly similar to prototypical ligand-bound MTANs (Fig. 11). Thus, the presence of a unique Trp (residue 48 within CT263, see *black star* in Fig. 6*B*) within the active site pocket might provide a stabilizing hydrophobic "platform" that could account for the lack of dimeric contacts typically present within the active site. The hypothesis that Trp-48 is sufficient to stabilize ligand binding is supported by the $CT263^{D161N}$-MTA structure (Fig. 9*C*). However, the presence of this novel active site side chain does not explain the fact that CT263 was unable to efficiently hydrolyze MTA and AdoHcy (Fig. 9, *B* and *C*). These two prototypical MTAN ligands lack the aromatic isophthalic moiety present within 6A6F. Thus, potential π-π bonding interactions with Trp-48 could properly position 6A6F for nucleophilic attack in the wild-type enzyme. Further studies exploring the contribution of Trp-48 to enzyme catalysis in CT263 are warranted.

Despite numerous similarities with Chlamydiaceae, including an obligate intracellular, biphasic developmental cycle, environmental Chlamydiales (*e.g. Protochlamydia, Parachlamydia, Waddlia,* and *Simkania*, among others) feature enhanced metabolic capabilities (61). Intriguingly, included among these additional pathways is a complete set of genes for the synthesis of MK through the traditional route (*e.g. menA-G*, Fig. 1). BLAST analysis of genes involved in the first four reactions of the futalosine pathway (including CT263) fails to identify any statistically significant targets within the environmental Chlamydiales. This indicates that only the traditional MK biosynthetic pathway is present within environmental Chlamydiales. As Chlamydiaceae and the environmental Chlamydiales are the closest evolutionary relatives to each other, the presence of differing pathways is extremely intriguing yet currently unexplained.

Chlamydia genomes have undergone a large degree of reductive evolution, Chlamydiaceae more so than environmental *Chlamydiales* given the 2–3 times smaller genomes found within that order (62). The environmental Chlamydiales are significantly more metabolically flexible than Chlamydiaceae, encoding additional genes involved in sugar utilization, a complete TCA cycle, and an expanded electron transport chain, among other pathways (61). As no organism has been found to simultaneously possess both MK biosynthetic pathways, it seems unlikely that the last common chlamydial ancestor (LCCA) encoded both pathways. It seems likely that the traditional MK pathway (*e.g. menA-G*) was encoded by the LCCA, as *men* gene homologs are found within both pathways. Upon diverging from the LCCA, Chlamydiaceae members could have independently acquired the first four genes of the futalosine pathway (and lost the corresponding *men* genes), potentially as a result of the differing degree of reliance on host metabolites and ATP for energy production between the two orders.

MTANs are required in a diverse array of biosynthetic pathways (37–39) that have yet to be implicated in *Chlamydia* (*e.g.* polyamine biosynthesis, quorum sensing, DNA methylation, etc.). Recently, however, Bonner *et al.* (63) have suggested that the synthesis of menaquinone, and thus enzymatic function of CT263, could be essential for Chlamydiaceae to maintain in a "persistent" state inside the host cell. Persistence is a reversible state of quiescence that Chlamydiaceae utilize as an immune evasion strategy (64). These authors speculated that the tryptophan (Trp) content of key proteins could dictate translational profiles during persistence as a means to respond to host cytosol Trp depletion (*e.g.* IFN-γ and indoleamine dioxygenase acti-

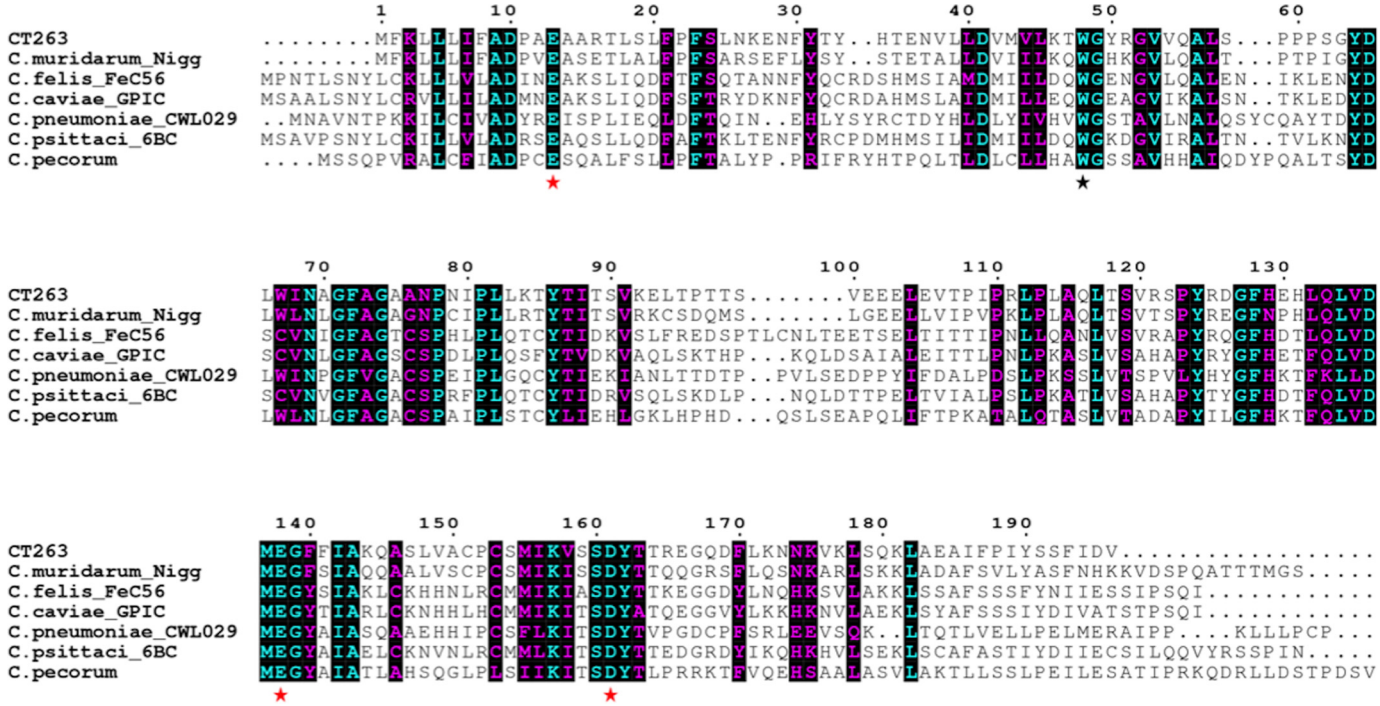

FIGURE 10. **Multiple sequence alignment of CT263 and Chlamydiaceae orthologs.** Limited structure-based alignment of CT263 and Chlamydiaceae orthologs was generated using ClustalW (23) and rendered with ESPRIPT (24). The *numbers* above the sequences correspond to *C. trachomatis* CT263. Residues are colored according to conservation (*cyan,* identical, and *purple,* similar) as judged by the BLOSUM62 matrix. *Stars* below the sequences correspond to catalytic triad amino acid side chains (*red*) or the Chlamydiaceae-specific aromatic active site residue Trp-48 (*black*). Accession numbers are detailed under "Experimental Procedures."

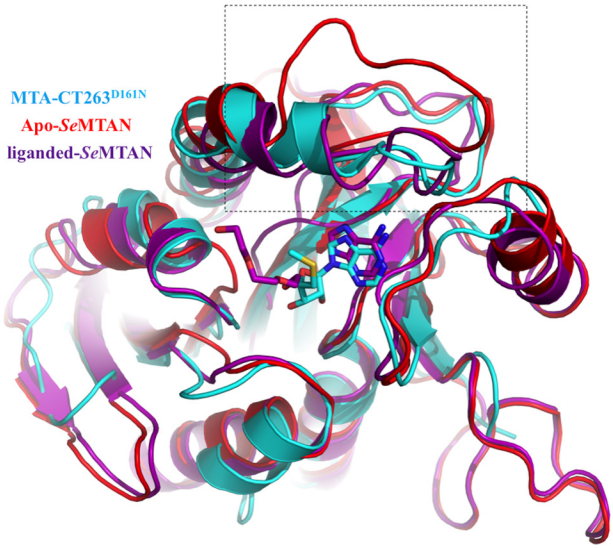

FIGURE 11. **CT263 structure naturally adopts closed-like conformation.** Structural comparison of CT263^{D161N}-MTA (*cyan*) and *S. enterica* MTAN open (*red*) and closed (*purple*) forms (PDB code: 4F1W), depicted in cartoon ribbon format. Respective bound ligands are shown as *balls-and-sticks (*MTA, *cyan* and ADE/TEG, *purple*). *Dashed box* highlights that CT263 active site is in a structurally similar conformation as the closed form of *S. enterica* MTAN.

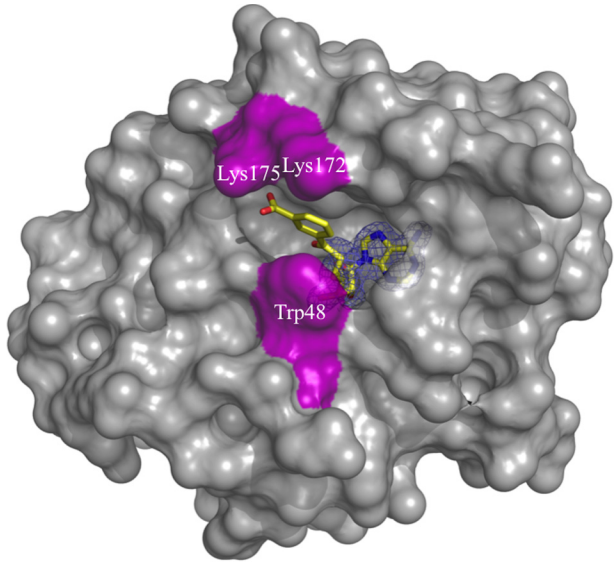

FIGURE 12. **Molecular model of AFL binding to CT263 active site.** 6-Amino-6-deoxyfutalosine (*yellow, balls-and-sticks*) was manually aligned (within COOT (19, 20)) on the MTA molecule present within the CT263^{D161N}-MTA cocrystal structure. CT263 is depicted in surface representation (20% transparency and colored *gray*). Side chains within potential interaction distance of the isophthalic moiety are colored *purple* and labeled. $2F_o - F_c$ electron density (countered at 1.0 σ) corresponding to bound MTA is presented, highlighting structural conservation between AFL and MTA.

vation). Of particular note to this hypothesis, the chorismate and MK pathways exhibit an extreme down-Trp selection in Chlamydiaceae, indicating potential importance to survival in the persistent state.

Our structural and kinetic observations indicate that CT263 (and orthologs in other chlamydial species) likely play an essential role in the menaquinone pathway. The crystal structure of CT263 revealed an active site with increased solvent exposure that resulted from the absence of the prototypical MTAN dimer interface. Furthermore, CT263 required only minimal structural rearrangements for substrate interaction. The structural information presented in

tandem with our emerging knowledge of MTAN-transition state analogs in prototypical MTANs (53–56), provides a promising starting point for the rational design of CT263-based anti-chlamydial therapeutics.

Acknowledgments—Use of the Advanced Photon Source was supported by the United States Department of Energy, Office of Science, Office of Basic Energy Sciences under Contact DE-AC02–06CH11357 and use of the IMCA-CAT beamline 17-ID by the companies of the Industrial Macromolecular Crystallography Association through a contract with the Hauptman-Woodward Medical Research Institute. Use of the COBRE-PSF Protein Structure Laboratory at Kansas University was supported by National Institutes of Health Grant 5P20RR017708-10 from the NCRR and Grant 8 P20 GM103420-10 from the NIGMS. We acknowledge the proteomics facility at Albert Einstein College of Medicine for conducting the mass spectroscopy analysis. We thank Brandon L. Garcia for critical reading and discussion of the manuscript. We thank Liang Tang and Haiyan Zhao for assistance with analytical size exclusion chromatography analysis.

REFERENCES

1. Kurosu, M., and Begari, E. (2010) Vitamin K2 in electron transport system: are enzymes involved in vitamin K2 biosynthesis promising drug targets? *Molecules* **15,** 1531–1553
2. Unden, G., and Bongaerts, J. (1997) Alternative respiratory pathways of *Escherichia coli*: energetics and transcriptional regulation in response to electron acceptors. *Biochim. Biophys. Acta* **1320,** 217–234
3. Furie, B., Bouchard, B. A., and Furie, B. C. (1999) Vitamin K-dependent biosynthesis of γ-carboxyglutamic acid. *Blood* **93,** 1798–1808
4. Bentley, R., and Meganathan, R. (1982) Biosynthesis of vitamin K (menaquinone) in bacteria. *Microbiol. Rev.* **46,** 241–280
5. Meganathan, R. (2001) Biosynthesis of menaquinone (vitamin K2) and ubiquinone (coenzyme Q): a perspective on enzymatic mechanisms. *Vitam. Horm.* **61,** 173–218
6. Hiratsuka, T., Furihata, K., Ishikawa, J., Yamashita, H., Itoh, N., Seto, H., and Dairi, T. (2008) An alternative menaquinone biosynthetic pathway operating in microorganisms. *Science* **321,** 1670–1673
7. Brooijmans, R., Smit, B., Santos, F., van Riel, J., de Vos, W. M., and Hugenholtz, J. (2009) Heme and menaquinone induced electron transport in lactic acid bacteria. *Microb. Cell Fact.* **8,** 28
8. Dairi, T. (2009) An alternative menaquinone biosynthetic pathway operating in microorganisms: an attractive target for drug discovery to pathogenic *Helicobacter* and *Chlamydia* strains. *J. Antibiot.* **62,** 347–352
9. Juul, N., Jensen, H., Hvid, M., Christiansen, G., and Birkelund, S. (2007) Characterization of *in vitro* chlamydial cultures in low-oxygen atmospheres. *J. Bacteriol.* **189,** 6723–6726
10. Stephens, R. S., Kalman, S., Lammel, C., Fan, J., Marathe, R., Aravind, L., Mitchell, W., Olinger, L., Tatusov, R. L., Zhao, Q., Koonin, E. V., and Davis, R. W. (1998) Genome sequence of an obligate intracellular pathogen of humans: *Chlamydia trachomatis*. *Science* **282,** 754–759
11. Zhi, X. Y., Yao, J. C., Tang, S. K., Li, Huang, Y., Li, H. W., and Li, W. J. (2014) The futalosine pathway played an important role in menaquinone biosynthesis during early prokaryote evolution. *Genome Biol. Evol.* **6,** 149–160
12. Geisbrecht, B. V., Bouyain, S., and Pop, M. (2006) An optimized system for expression and purification of secreted bacterial proteins. *Protein Expr. Purif.* **46,** 23–32
13. Doublié, S. (2007) Production of selenomethionyl proteins in prokaryotic and eukaryotic expression systems. *Methods Mol. Biol.* **363,** 91–108
14. Kabsch, W. (2010) XDS. *Acta Crystallogr. D Biol. Crystallogr.* **66,** 125–132
15. Evans, P. R. (2011) An introduction to data reduction: space-group determination, scaling and intensity statistics. *Acta Crystallogr. D Biol. Crystallogr.* **67,** 282–292
16. Collaborative Computational Project, Number 4 (1994) The CCP4 Suite: programs for protein crystallography. *Acta Crystallogr. D Biol. Crystallogr.* **50,** 760–763
17. Adams, P. D., Grosse-Kunstleve, R. W., Hung, L. W., Ioerger, T. R., McCoy, A. J., Moriarty, N. W., Read, R. J., Sacchettini, J. C., Sauter, N. K., and Terwilliger, T. C. (2002) PHENIX: building new software for automated crystallographic structure determination. *Acta Crystallogr. D Biol. Crystallogr.* **58,** 1948–1954
18. Adams, P. D., Afonine, P. V., Bunkóczi, G., Chen, V. B., Davis, I. W., Echols, N., Headd, J. J., Hung, L. W., Kapral, G. J., Grosse-Kunstleve, R. W., McCoy, A. J., Moriarty, N. W., Oeffner, R., Read, R. J., Richardson, D. C., Richardson, J. S., Terwilliger, T. C., and Zwart, P. H. (2010) PHENIX: a comprehensive Python-based system for macromolecular structure solution. *Acta Crystallogr. D Biol. Crystallogr.* **66,** 213–221
19. Emsley, P., and Cowtan, K. (2004) Coot: model-building tools for molecular graphics. *Acta Crystallogr. D Biol. Crystallogr.* **60,** 2126–2132
20. Emsley, P., Lohkamp, B., Scott, W. G., and Cowtan, K. (2010) Features and development of Coot. *Acta Crystallogr. D Biol. Crystallogr.* **66,** 486–501
21. Painter, J., and Merritt, E. A. (2006) Optimal description of a protein structure in terms of multiple groups undergoing TLS motion. *Acta Crystallogr. D Biol. Crystallogr.* **62,** 439–450
22. Sturm, M. B., and Schramm, V. L. (2009) Detecting ricin: sensitive luminescent assay for ricin A-chain ribosome depurination kinetics. *Anal. Chem.* **81,** 2847–2853
23. Thompson, J. D., Higgins, D. G., and Gibson, T. J. (1994) CLUSTAL W: improving the sensitivity of progressive multiple sequence alignment through sequence weighting, position-specific gap penalties and weight matrix choice. *Nucleic Acids Res.* **22,** 4673–4680
24. Gouet, P., Courcelle, E., Stuart, D., and Métoz, F. (1999) ESPript: analysis of multiple sequence alignments in PostScript. *Bioinformatics* **15,** 305–308
25. Zemla, A. (2003) LGA: A method for finding 3D similarities in protein structures. *Nucleic Acids Res.* **31,** 3370–3374
26. Bernstein, F. C., Koetzle, T. F., Williams, G. J., Meyer, E. F., Jr., Brice, M. D., Rodgers, J. R., Kennard, O., Shimanouchi, T., and Tasumi, M. (1977) The Protein Data Bank. A computer-based archival file for macromolecular structures. *Eur. J. Biochem.* **80,** 319–324
27. DeLano, W. L. (2002) *The PyMOL Molecular Graphics System,* DeLano Scientific LLC, San Carlos, CA
28. Rocchia, W., Sridharan, S., Nicholls, A., Alexov, E., Chiabrera, A., and Honig, B. (2002) Rapid grid-based construction of the molecular surface and the use of induced surface charge to calculate reaction field energies: applications to the molecular systems and geometric objects. *J. Comput. Chem.* **23,** 128–137
29. Glaser, F., Pupko, T., Paz, I., Bell, R. E., Bechor-Shental, D., Martz, E., and Ben-Tal, N. (2003) ConSurf: identification of functional regions in proteins by surface-mapping of phylogenetic information. *Bioinformatics* **19,** 163–164
30. Omsland, A., Sager, J., Nair, V., Sturdevant, D. E., and Hackstadt, T. (2012) Developmental stage-specific metabolic and transcriptional activity of *Chlamydia trachomatis* in an axenic medium. *Proc. Natl. Acad. Sci. U.S.A.* **109,** 19781–19785
31. Binet, R., Fernandez, R. E., Fisher, D. J., and Maurelli, A. T. (2011) Identification and characterization of the *Chlamydia trachomatis* L2 *S*-adenosylmethionine transporter. *MBio* **2,** e00051–e00011
32. Albrecht, M., Sharma, C. M., Reinhardt, R., Vogel, J., and Rudel, T. (2010) Deep sequencing-based discovery of the *Chlamydia trachomatis* transcriptome. *Nucleic Acids Res.* **38,** 868–877
33. Zhang, Y. (2008) I-TASSER server for protein 3D structure prediction. *BMC Bioinformatics* **9,** 40
34. Zhang, Y. (2009) I-TASSER: fully automated protein structure prediction in CASP8. *Proteins* **77,** Suppl. 9, 100–113
35. Roy, A., Kucukural, A., and Zhang, Y. (2010) I-TASSER: a unified platform for automated protein structure and function prediction. *Nat. Protoc.* **5,** 725–738
36. Zhang, Y., and Skolnick, J. (2004) Scoring function for automated assessment of protein structure template quality. *Proteins* **57,** 702–710
37. Miller, C. H., and Duerre, J. A. (1968) *S*-Ribosylhomocysteine cleavage enzyme from *Escherichia coli*. *J. Biol. Chem.* **243,** 92–97

38. Choi-Rhee, E., and Cronan, J. E. (2005) A nucleosidase required for *in vivo* function of the *S*-adenosyl-L-methionine radical enzyme, biotin synthase. *Chem. Biol.* **12,** 589–593
39. Della Ragione, F., Porcelli, M., Cartenì-Farina, M., Zappia, V., and Pegg, A. E. (1985) *Escherichia coli S*-adenosylhomocysteine/5′-methylthioadenosine nucleosidase. Purification, substrate specificity and mechanism of action. *Biochem. J.* **232,** 335–341
40. Allart, B., Gatel, M., Guillerm, D., and Guillerm, G. (1998) The catalytic mechanism of adenosylhomocysteine/methylthioadenosine nucleosidase from *Escherichia coli*–chemical evidence for a transition state with a substantial oxocarbenium character. *Eur. J. Biochem.* **256,** 155–162
41. Lee, J. E., Smith, G. D., Horvatin, C., Huang, D. J., Cornell, K. A., Riscoe, M. K., and Howell, P. L. (2005) Structural snapshots of MTA/AdoHcy nucleosidase along the reaction coordinate provide insights into enzyme and nucleoside flexibility during catalysis. *J. Mol. Biol.* **352,** 559–574
42. Lee, J. E., Cornell, K. A., Riscoe, M. K., and Howell, P. L. (2003) Structure of *Escherichia coli* 5′-methylthioadenosine/*S*-adenosylhomocysteine nucleosidase inhibitor complexes provide insight into the conformational changes required for substrate binding and catalysis. *J. Biol. Chem.* **278,** 8761–8770
43. Singh, V., Lee, J. E., Núñez, S., Howell, P. L., and Schramm, V. L. (2005) Transition state structure of 5′-methylthioadenosine/*S*-adenosylhomocysteine nucleosidase from *Escherichia coli* and its similarity to transition state analogues. *Biochemistry* **44,** 11647–11659
44. Sufrin, J. R., Meshnick, S. R., Spiess, A. J., Garofalo-Hannan, J., Pan, X. Q., and Bacchi, C. J. (1995) Methionine recycling pathways and antimalarial drug design. *Antimicrob. Agents Chemother.* **39,** 2511–2515
45. Parveen, N., and Cornell, K. A. (2011) Methylthioadenosine/*S*-adenosylhomocysteine nucleosidase, a critical enzyme for bacterial metabolism. *Mol. Microbiol.* **79,** 7–20
46. Raina, A., Tuomi, K., and Pajula, R. L. (1982) Inhibition of the synthesis of polyamines and macromolecules by 5′-methylthioadenosine and 5′-alkylthiotubercidins in BHK21 cells. *Biochem. J.* **204,** 697–703
47. Pajula, R. L., and Raina, A. (1979) Methylthioadenosine, a potent inhibitor of spermine synthase from bovine brain. *FEBS Lett.* **99,** 343–345
48. Bar-Even, A., Noor, E., Savir, Y., Liebermeister, W., Davidi, D., Tawfik, D. S., and Milo, R. (2011) The moderately efficient enzyme: evolutionary and physicochemical trends shaping enzyme parameters. *Biochemistry* **50,** 4402–4410
49. Zeyhle, P., Bauer, J. S., Kalinowski, J., Shin-ya, K., Gross, H., and Heide, L. (2014) Genome-based discovery of a novel membrane-bound 1,6-dihydroxyphenazine prenyltransferase from a marine actinomycete. *PloS one* **9,** e99122
50. Yu, C. M., Mun, S., and Wang, N. H. (2006) Theoretical analysis of the effects of reversible dimerization in size exclusion chromatography. *J. Chromatogr. A* **1132,** 99–108
51. Holm, L., and Rosenström, P. (2010) Dali server: conservation mapping in 3D. *Nucleic Acids Res.* **38,** W545–W549
52. Mishra, V., and Ronning, D. R. (2012) Crystal structures of the Helicobacter pylori MTAN enzyme reveal specific interactions between *S*-adenosylhomocysteine and the 5′-alkylthio binding subsite. *Biochemistry* **51,** 9763–9772
53. Wang, S., Haapalainen, A. M., Yan, F., Du, Q., Tyler, P. C., Evans, G. B., Rinaldo-Matthis, A., Brown, R. L., Norris, G. E., Almo, S. C., and Schramm, V. L. (2012) A picomolar transition state analogue inhibitor of MTAN as a specific antibiotic for *Helicobacter pylori*. *Biochemistry* **51,** 6892–6894
54. Haapalainen, A. M., Thomas, K., Tyler, P. C., Evans, G. B., Almo, S. C., and Schramm, V. L. (2013) *Salmonella enterica* MTAN at 1.36 A resolution: a structure-based design of tailored transition state analogs. *Structure* **21,** 963–974
55. Gutierrez, J. A., Crowder, T., Rinaldo-Matthis, A., Ho, M. C., Almo, S. C., and Schramm, V. L. (2009) Transition state analogs of 5′-methylthioadenosine nucleosidase disrupt quorum sensing. *Nat. Chem. Biol.* **5,** 251–257
56. Lee, J. E., Singh, V., Evans, G. B., Tyler, P. C., Furneaux, R. H., Cornell, K. A., Riscoe, M. K., Schramm, V. L., and Howell, P. L. (2005) Structural rationale for the affinity of pico- and femtomolar transition state analogues of *Escherichia coli* 5′-methylthioadenosine/*S*-adenosylhomocysteine nucleosidase. *J. Biol. Chem.* **280,** 18274–18282
57. Kim, R. Q., Offen, W. A., Davies, G. J., and Stubbs, K. A. (2014) Structural enzymology of *Helicobacter pylori* methylthioadenosine nucleosidase in the futalosine pathway. *Acta Crystallogr. D Biol. Crystallogr.* **70,** 177–185
58. Lee, J. E., Cornell, K. A., Riscoe, M. K., and Howell, P. L. (2001) Structure of *E. coli* 5′-methylthioadenosine/*S*-adenosylhomocysteine nucleosidase reveals similarity to the purine nucleoside phosphorylases. *Structure* **9,** 941–953
59. Ronning, D. R., Iacopelli, N. M., and Mishra, V. (2010) Enzyme-ligand interactions that drive active site rearrangements in the Helicobacter pylori 5′-methylthioadenosine/*S*-adenosylhomocysteine nucleosidase. *Protein Sci.* **19,** 2498–2510
60. Siu, K. K., Lee, J. E., Smith, G. D., Horvatin-Mrakovcic, C., and Howell, P. L. (2008) Structure of *Staphylococcus aureus* 5′-methylthioadenosine/*S*-adenosylhomocysteine nucleosidase. *Acta Crystallogr. Sect. F Struct. Biol. Cryst. Commun.* **64,** 343–350
61. Omsland, A., Sixt, B. S., Horn, M., and Hackstadt, T. (2014) Chlamydial metabolism revisited: interspecies metabolic variability and developmental stage-specific physiologic activities. *FEMS Microbiol. Rev.* **38,** 779–801
62. Collingro, A., Tischler, P., Weinmaier, T., Penz, T., Heinz, E., Brunham, R. C., Read, T. D., Bavoil, P. M., Sachse, K., Kahane, S., Friedman, M. G., Rattei, T., Myers, G. S., and Horn, M. (2011) Unity in variety–the pangenome of the chlamydiae. *Mol. Biol. Evol.* **28,** 3253–3270
63. Bonner, C. A., Byrne, G. I., and Jensen, R. A. (2014) *Chlamydia* exploit the mammalian tryptophan-depletion defense strategy as a counter-defensive cue to trigger a survival state of persistence. *Front. Cell. Infect. Microbiol.* **4,** 17
64. Beatty, W. L., Morrison, R. P., and Byrne, G. I. (1994) Persistent chlamydiae: from cell culture to a paradigm for chlamydial pathogenesis. *Microbiol. Rev.* **58,** 686–699
65. Evans, P. (2012) Biochemistry. Resolving some old problems in protein crystallography. *Science* **336,** 986–987
66. Evans, P. (2006) Scaling and assessment of data quality. *Acta Crystallogr. D Biol. Crystallogr.* **62,** 72–82
67. Diederichs, K., and Karplus, P. A. (1997) Improved R-factors for diffraction data analysis in macromolecular crystallography. *Nat. Struct. Biol.* **4,** 269–275
68. Weiss, M. S. (2001) Global indicators of x-ray data quality. *J. Appl. Crystallogr.* **34,** 130–135
69. Karplus, P. A., and Diederichs, K. (2012) Linking crystallographic model and data quality. *Science* **336,** 1030–1033

Structural and Biochemical Characterization of *Chlamydia trachomatis* Hypothetical Protein CT263 Supports That Menaquinone Synthesis Occurs through the Futalosine Pathway

Michael L. Barta, Keisha Thomas, Hongling Yuan, Scott Lovell, Kevin P. Battaile, Vern L. Schramm and P. Scott Hefty

J. Biol. Chem. 2014, 289:32214-32229.
doi: 10.1074/jbc.M114.594325 originally published online September 24, 2014
